Supplemental information

Dynamically preferred state with strong

electronic fluctuations from electrochemical

synthesis of sodium manganate

Xi Chen, Yichao Wang, Yiping Wang, Rebecca L. Dally, Kamila Wiaderek, Tianyu Qiao, Jue Liu, Enyuan Hu, Kenneth Burch, Jeffrey W. Lynn, and Xin Li
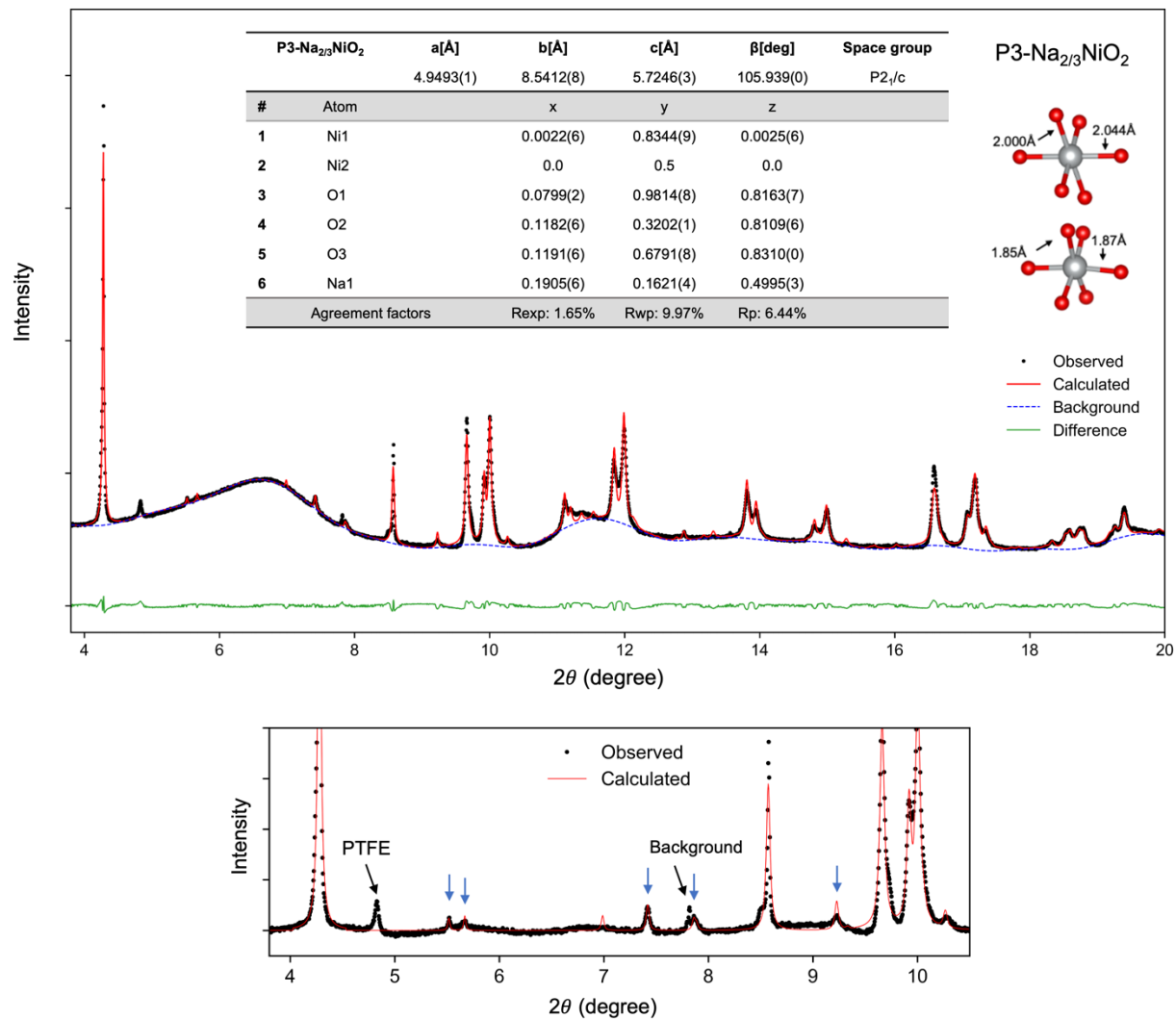
P3-Na$_{2/3}$NiO$_2$		a[Å]	b[Å]	c[Å]	β[deg]	Space group
		4.9493(1)	8.5412(8)	5.7246(3)	105.939(0)	P2$_1$/c
#	Atom		x	y	z	
1	Ni1		0.0022(6)	0.8344(9)	0.0025(6)	
2	Ni2		0.0	0.5	0.0	
3	O1		0.0799(2)	0.9814(8)	0.8163(7)	
4	O2		0.1182(6)	0.3202(1)	0.8109(6)	
5	O3		0.1191(6)	0.6791(8)	0.8310(0)	
6	Na1		0.1905(6)	0.1621(4)	0.4995(3)	
	Agreement factors		Rexp: 1.65%	Rwp: 9.97%	Rp: 6.44%	

P3-Na$_{2/3}$NiO$_2$

2.000Å 2.044Å

1.85Å 1.87Å

- Observed
- Calculated
- Background
- Difference

PTFE

Background

Figure S1. *In-situ* synchrotron XRD and Rietveld refinement for Na$_{2/3}$NiO$_2$. The broad background is from the scattering induced by various components in the *in situ* battery cell, including glass fiber separator, liquid electrolyte of 1M NaPF6 in 1:1 EC:DEC and amorphous glass windows. (bottom) Enlarged region of the top figure to more clearly show the superstructure peaks and their refinement. The experimentally identified superstructure peaks are labelled by vertical blue arrows. The PTFE peak and a background peak are marked by black arrows with an inclined angle to the vertical direction. The broad background from *in situ* XRD cell background is also subtracted in the bottom plot.
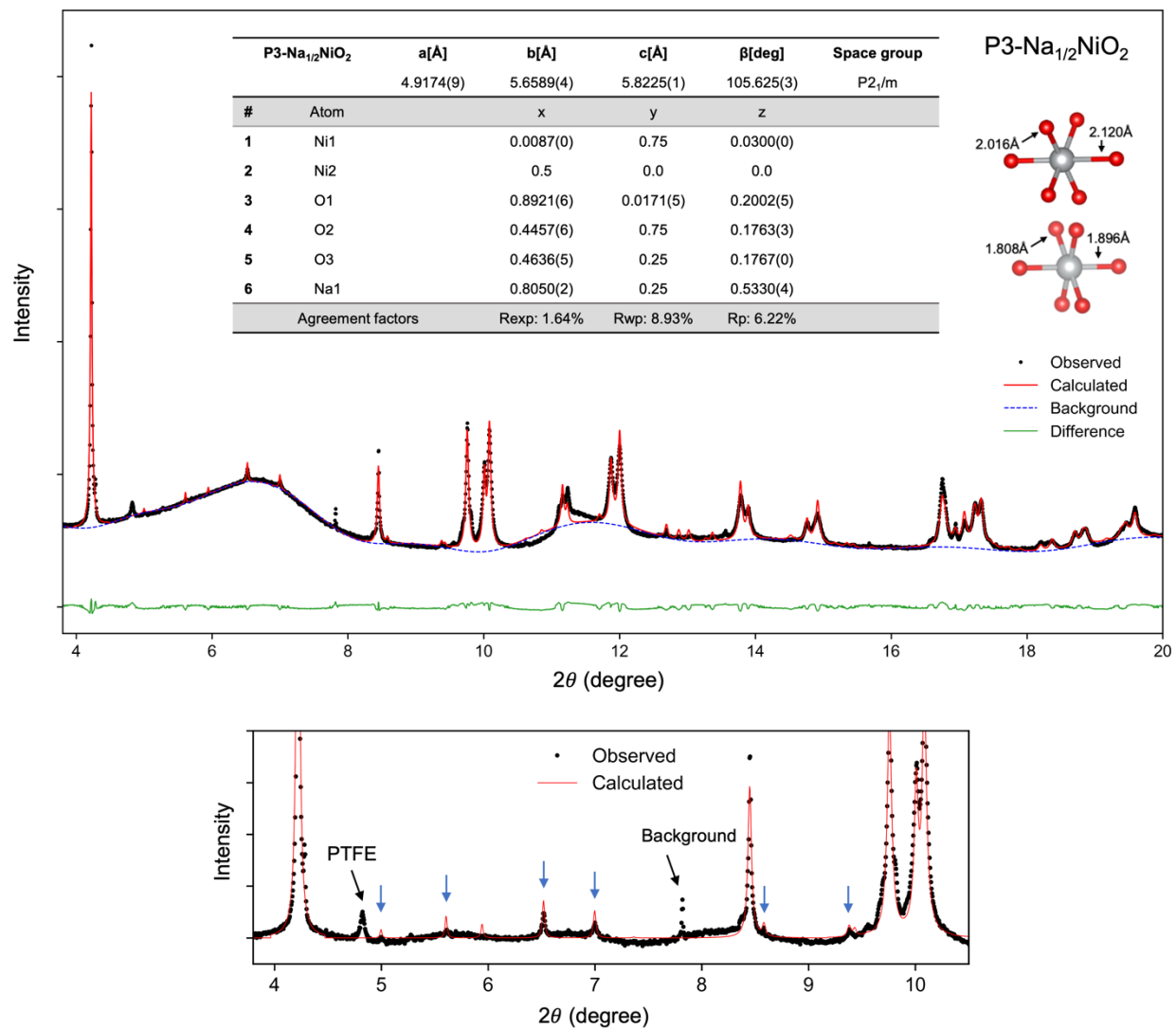
The following data table appears within the figure:

P3-Na$_{1/2}$NiO$_2$	a[Å]	b[Å]	c[Å]	β[deg]	Space group
	4.9174(9)	5.6589(4)	5.8225(1)	105.625(3)	P2$_1$/m

#	Atom	x	y	z
1	Ni1	0.0087(0)	0.75	0.0300(0)
2	Ni2	0.5	0.0	0.0
3	O1	0.8921(6)	0.0171(5)	0.2002(5)
4	O2	0.4457(6)	0.75	0.1763(3)
5	O3	0.4636(5)	0.25	0.1767(0)
6	Na1	0.8050(2)	0.25	0.5330(4)
	Agreement factors	Rexp: 1.64%	Rwp: 8.93%	Rp: 6.22%

Figure S2. *In-situ* **synchrotron XRD and Rietveld refinement for Na$_{1/2}$NiO$_2$.** (bottom) Enlarged region with the experimentally identified superstructure peaks labelled by vertical blue arrows. The broad background is subtracted in the bottom plot.
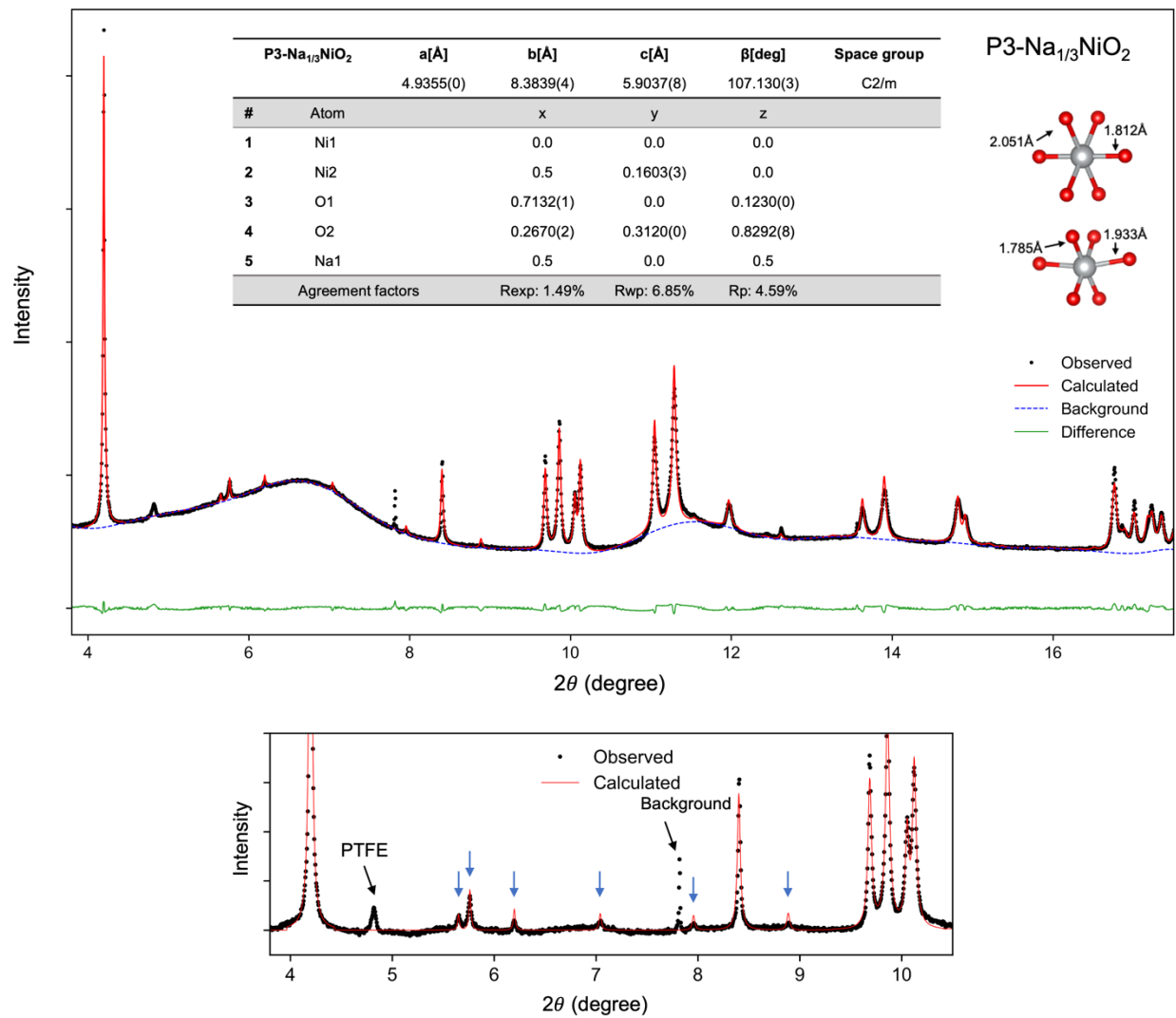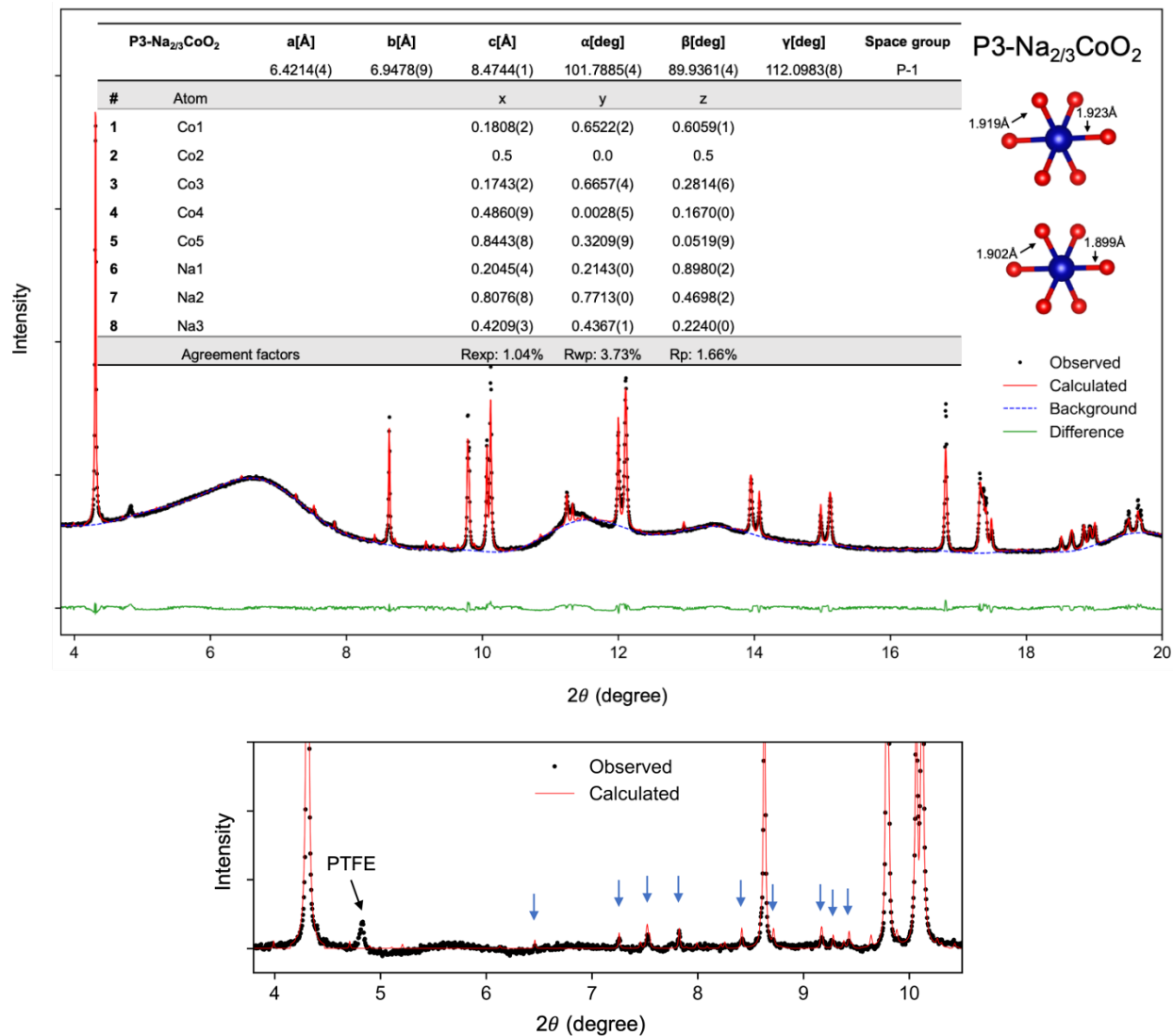
Figure S3. *In-situ* synchrotron XRD and Rietveld refinement for Na$_{1/3}$NiO$_2$. (bottom) Enlarged region with the experimentally identified superstructure peaks labelled by vertical blue arrows. The broad background is subtracted in the bottom plot.
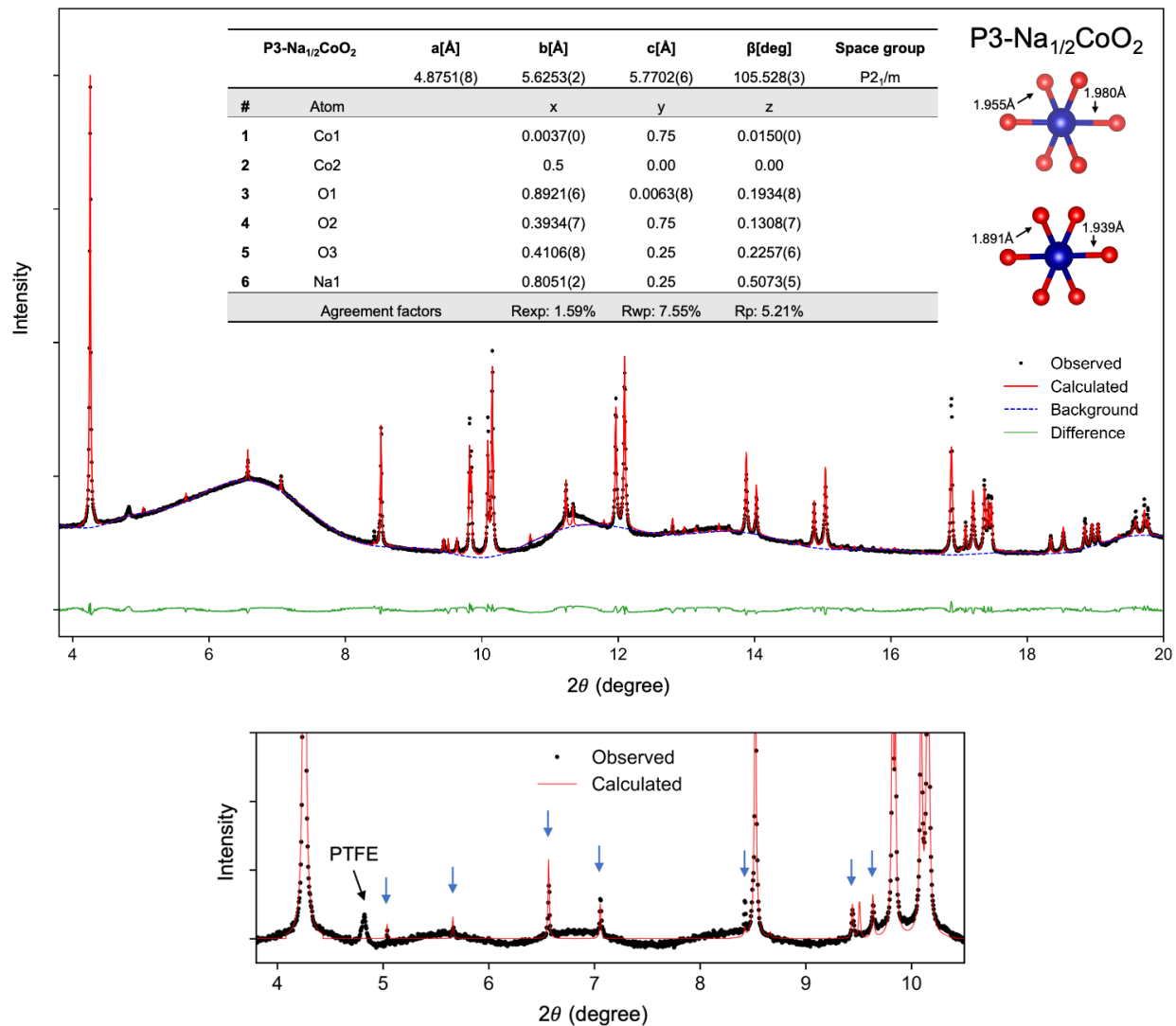
Figure S4. *In-situ* **synchrotron XRD and Rietveld refinement for Na$_{2/3}$CoO$_2$.** Refined with the 2% restriction of relative internal coordinate change starting from the DFT structure. (bottom) Enlarged region with the experimentally identified superstructure peaks labelled by vertical blue arrows. The broad background is subtracted in the bottom plot.
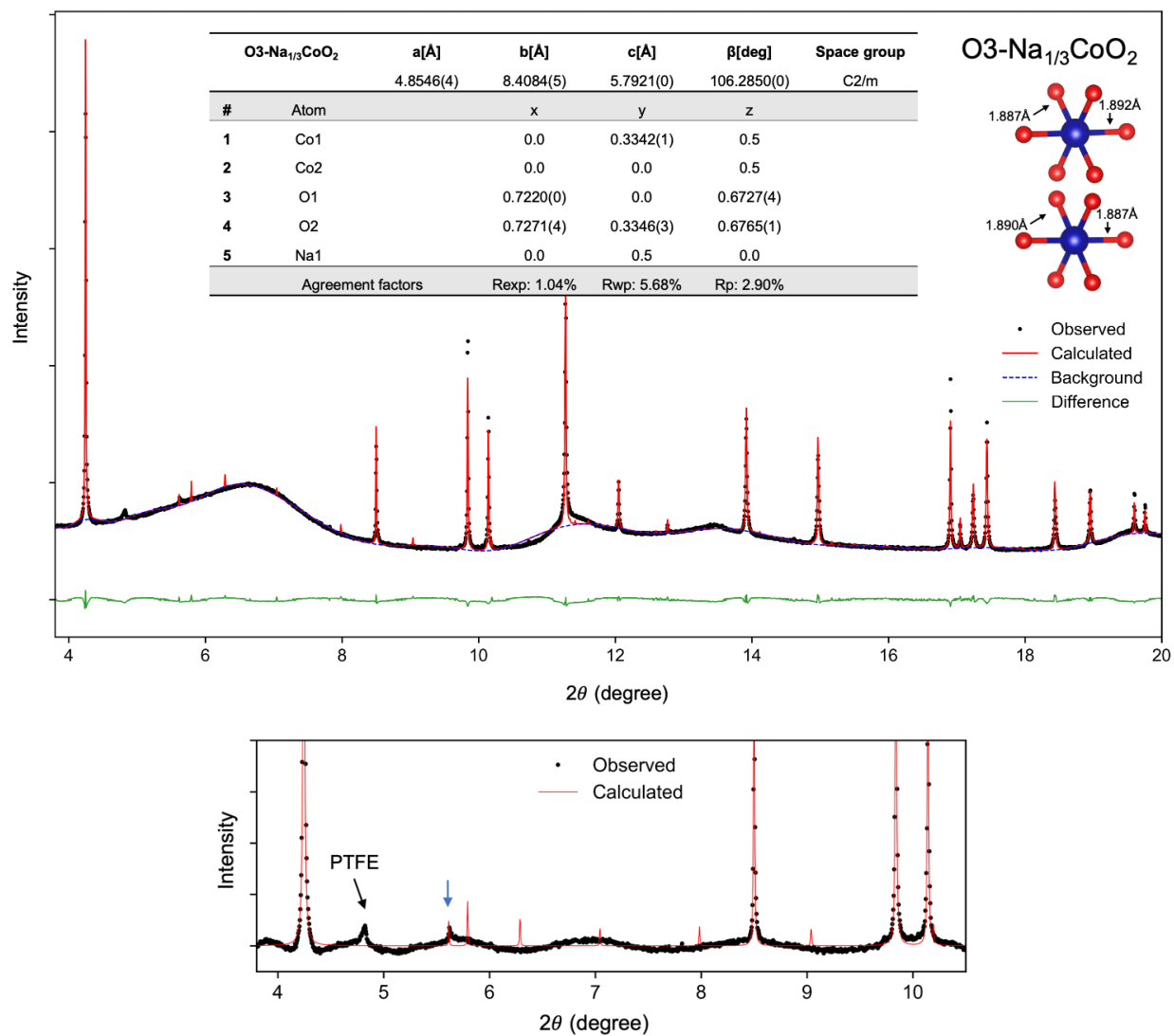
Figure S5. *In-situ* **synchrotron XRD and Rietveld refinement for Na$_{1/2}$CoO$_2$.** (bottom) Enlarged region with the experimentally identified superstructure peaks labelled by vertical blue arrows. The broad background is subtracted in the bottom plot.

O3-Na$_{1/3}$CoO$_2$		a[Å]	b[Å]	c[Å]	β[deg]	Space group
		4.8546(4)	8.4084(5)	5.7921(0)	106.2850(0)	C2/m
#	Atom		x	y	z	
1	Co1		0.0	0.3342(1)	0.5	
2	Co2		0.0	0.0	0.5	
3	O1		0.7220(0)	0.0	0.6727(4)	
4	O2		0.7271(4)	0.3346(3)	0.6765(1)	
5	Na1		0.0	0.5	0.0	
	Agreement factors		Rexp: 1.04%	Rwp: 5.68%	Rp: 2.90%	

Figure S6. *In-situ* **synchrotron XRD and Rietveld refinement for Na$_{1/3}$CoO$_2$.** Refined with the 2% restriction of relative internal coordinate change starting from the DFT structure. (bottom) Enlarged region with the experimentally identified superstructure peaks labelled by vertical blue arrows. The broad background is subtracted in the bottom plot. This ordering shows weak superstructure peak signals in the *in-situ* XRD pattern.
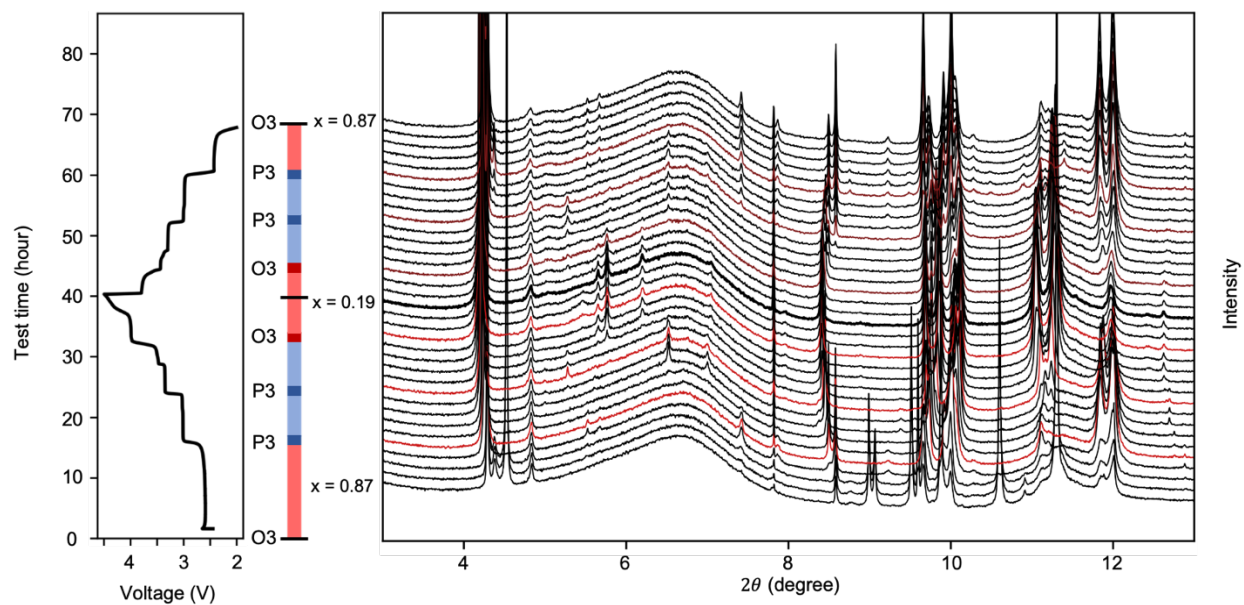
Figure S7. *In-situ* **synchrotron XRD measurement of Na$_x$NiO$_2$ with an electrochemical charge and discharge rate of C/50.** Each XRD scan corresponds to 1% of Na composition change. The O3 and P3 ordered single-phase regions are marked by darker red and darker blue in the phase evolution bar. Lighter red and lighter blue regions in the bar correspond to two-phase regions. The XRD scans corresponding to the ordered single-phase regions are also highlighted in red in the right figure.
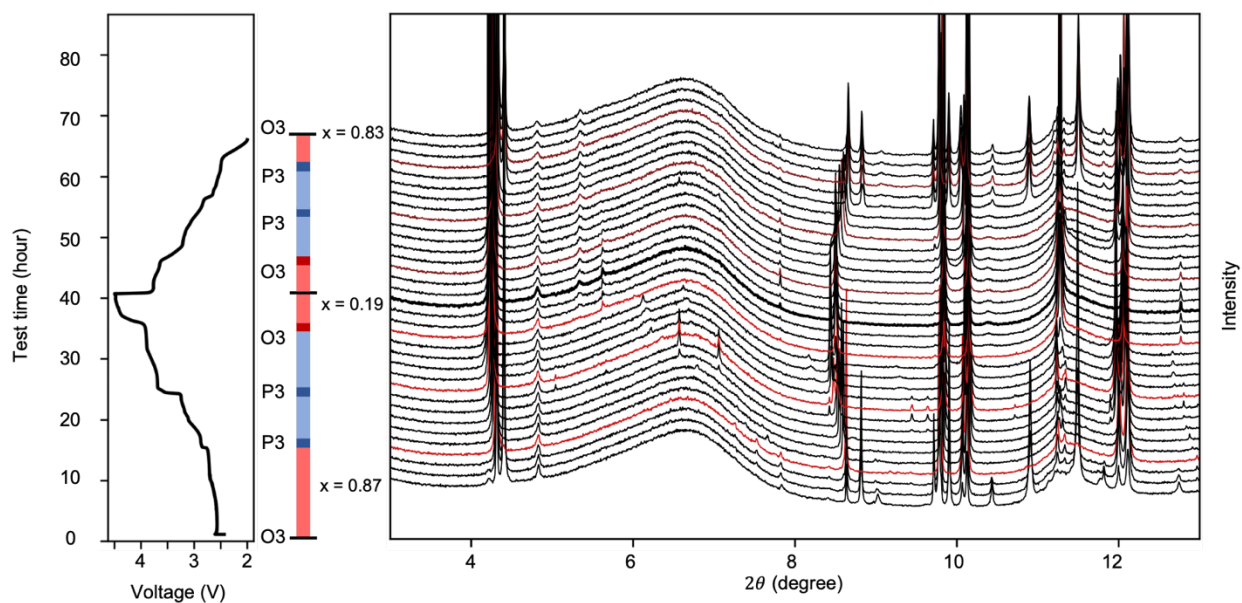
Figure S8. *In-situ* **synchrotron XRD measurement of Na$_x$CoO$_2$ at C/50 rate.** Each scan corresponds to 1% of Na composition change. The O3 and P3 ordered single-phase regions are marked by darker red and darker blue. Lighter red and lighter blue regions correspond to two-phase regions. The XRD scans corresponding to the ordered single-phase regions are also highlighted in red.
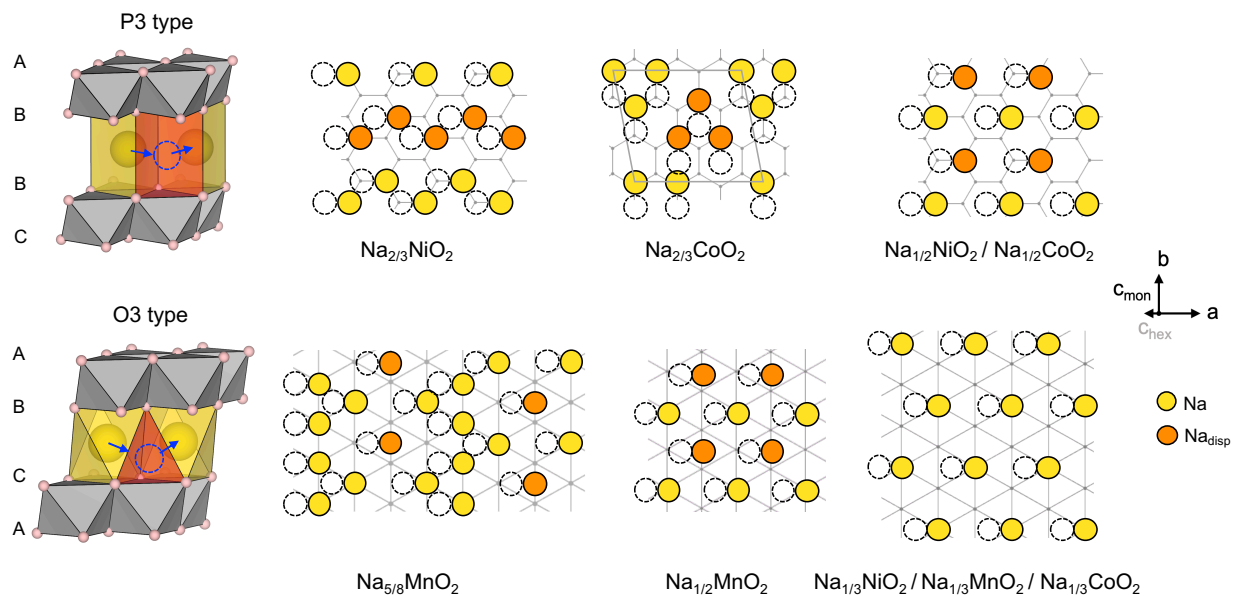
Figure S9. **Structure evolution of Na$_x$NiO$_2$, Na$_x$CoO$_2$, Na$_x$MnO$_2$ solved from *in situ* SXRD.** Definition of the P3 and O3 type TMO$_2$ stacking (3D model on the leftmost) and the stacking of Na (2D projection) in the major ordering structures presented in Fig. 1 of the Main Text. The 2D projections are along hexagonal-*c* crystallographic direction.
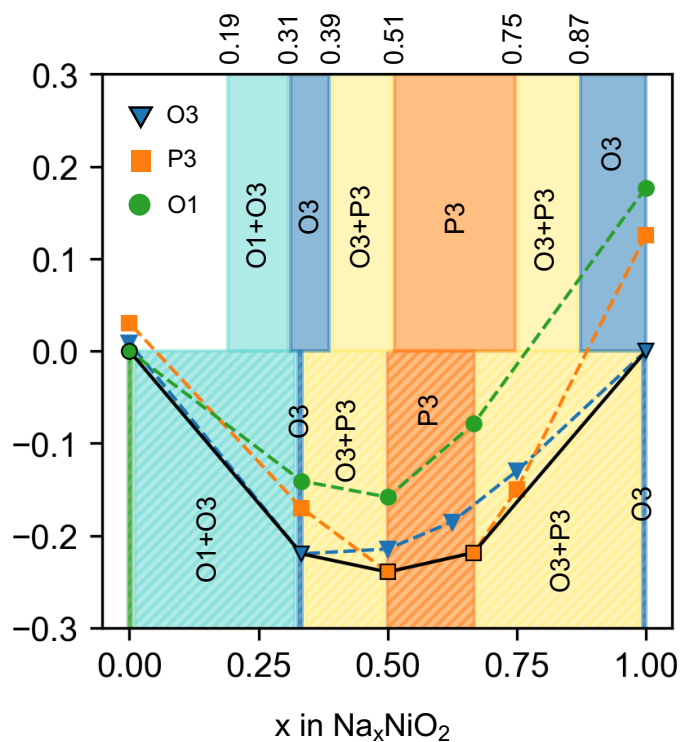
Figure S10. Measured and calculated phase diagrams of Na_xNiO_2. All the DFT predicted major ground state orderings at discrete x values for Na_xNiO_2 agree with experimental SXRD refinements (Fig. S1 to S3). The phase boundaries given by the solid shaded areas (top part) are determined by *in situ* SXRD (Fig. S7) and the shaded areas with skewed lines (bottom part) are those determined by the data points from DFT computations. The numbers on the top x-axis of the figure are the boundary compositions obtained from *in situ* SXRD (Fig. S7).
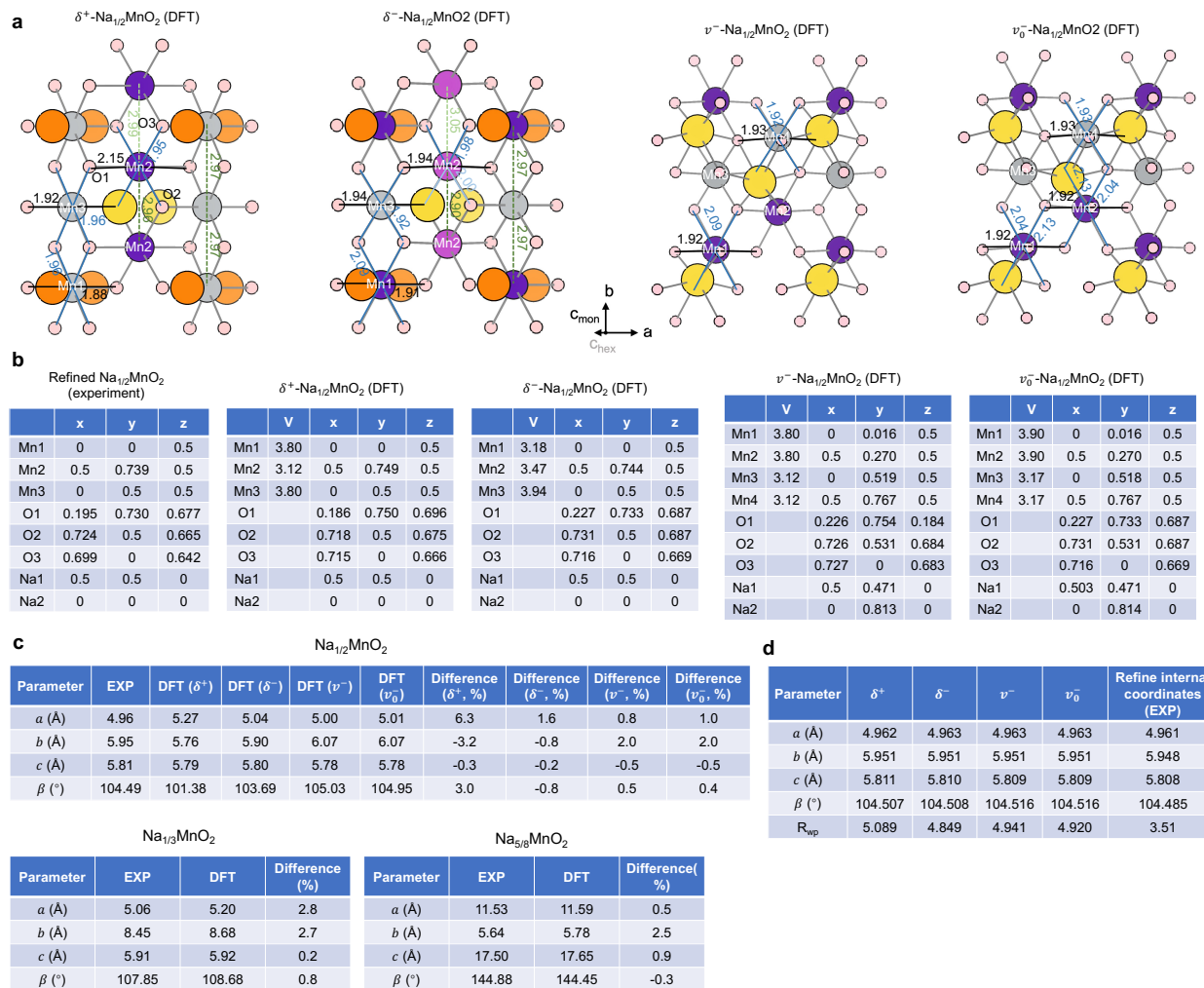
b

Refined Na$_{1/2}$MnO$_2$ (experiment)

	x	y	z
Mn1	0	0	0.5
Mn2	0.5	0.739	0.5
Mn3	0	0.5	0.5
O1	0.195	0.730	0.677
O2	0.724	0.5	0.665
O3	0.699	0	0.642
Na1	0.5	0.5	0
Na2	0	0	0

δ^+-Na$_{1/2}$MnO$_2$ (DFT)

	V	x	y	z
Mn1	3.80	0	0	0.5
Mn2	3.12	0.5	0.749	0.5
Mn3	3.80	0	0.5	0.5
O1		0.186	0.750	0.696
O2		0.718	0.5	0.675
O3		0.715	0	0.666
Na1		0.5	0.5	0
Na2		0	0	0

δ^--Na$_{1/2}$MnO$_2$ (DFT)

	V	x	y	z
Mn1	3.18	0	0	0.5
Mn2	3.47	0.5	0.744	0.5
Mn3	3.94	0	0.5	0.5
O1		0.227	0.733	0.687
O2		0.731	0.5	0.687
O3		0.716	0	0.669
Na1		0.5	0.5	0
Na2		0	0	0

ν^--Na$_{1/2}$MnO$_2$ (DFT)

	V	x	y	z
Mn1	3.80	0	0.016	0.5
Mn2	3.80	0.5	0.270	0.5
Mn3	3.12	0	0.519	0.5
Mn4	3.12	0.5	0.767	0.5
O1		0.226	0.754	0.184
O2		0.726	0.531	0.684
O3		0.727	0	0.683
Na1		0.5	0.471	0
Na2		0	0.813	0

ν_0^--Na$_{1/2}$MnO$_2$ (DFT)

	V	x	y	z
Mn1	3.90	0	0.016	0.5
Mn2	3.90	0.5	0.270	0.5
Mn3	3.17	0	0.518	0.5
Mn4	3.17	0.5	0.767	0.5
O1		0.227	0.733	0.687
O2		0.731	0.531	0.687
O3		0.716	0	0.669
Na1		0.503	0.471	0
Na2		0	0.814	0

c

Na$_{1/2}$MnO$_2$

Parameter	EXP	DFT (δ^+)	DFT (δ^-)	DFT (ν^-)	DFT (ν_0^-)	Difference (δ^+, %)	Difference (δ^-, %)	Difference (ν^-, %)	Difference (ν_0^-, %)
a (Å)	4.96	5.27	5.04	5.00	5.01	6.3	1.6	0.8	1.0
b (Å)	5.95	5.76	5.90	6.07	6.07	-3.2	-0.8	2.0	2.0
c (Å)	5.81	5.79	5.80	5.78	5.78	-0.3	-0.2	-0.5	-0.5
β (°)	104.49	101.38	103.69	105.03	104.95	3.0	-0.8	0.5	0.4

Na$_{1/3}$MnO$_2$

Parameter	EXP	DFT	Difference (%)
a (Å)	5.06	5.20	2.8
b (Å)	8.45	8.68	2.7
c (Å)	5.91	5.92	0.2
β (°)	107.85	108.68	0.8

Na$_{5/8}$MnO$_2$

Parameter	EXP	DFT	Difference (%)
a (Å)	11.53	11.59	0.5
b (Å)	5.64	5.78	2.5
c (Å)	17.50	17.65	0.9
β (°)	144.88	144.45	-0.3

d

Parameter	δ^+	δ^-	ν^-	ν_0^-	Refine internal coordinates (EXP)
a (Å)	4.962	4.963	4.963	4.963	4.961
b (Å)	5.951	5.951	5.951	5.951	5.948
c (Å)	5.811	5.810	5.809	5.809	5.808
β (°)	104.507	104.508	104.516	104.516	104.485
R_{wp}	5.089	4.849	4.941	4.920	3.51

Figure S11. Lattice parameters, bond lengths and internal coordinates of δ^+, δ^-, ν^- and ν_0^- structures. (a) δ^+, δ^-, ν^- and ν_0^- structures of Na$_{1/2}$MnO$_2$ from DFT relaxations at experimental lattice parameters. The numbers show the length (in Å) of each Mn-O bond, as well as the Mn-Mn distances along *b* direction. The corresponding connection lines between atoms are marked with the same color as the numbers. (b) The internal coordinates of Na$_{1/2}$MnO$_2$ refined from *in-situ* SXRD experiment, and the four x = 1/2 states from DFT relaxations. The valences of the Mn ions are also labeled in the "V" column for the DFT cases. (c) The lattice parameters obtained from *in-situ* SXRD refinement (EXP) and DFT relaxed energy minimum states (DFT) for x = 1/3, 5/8, and the four candidate states for x = 1/2. The difference (%) between calculated and experimental ones are also presented. (d) Refined lattice parameters and goodness of fit (R_{wp}) by fixing internal coordinates from δ^-, δ^-, ν^- and ν_0^- structures at x = 1/2, compared with the result from fully refined internal coordinates (EXP).

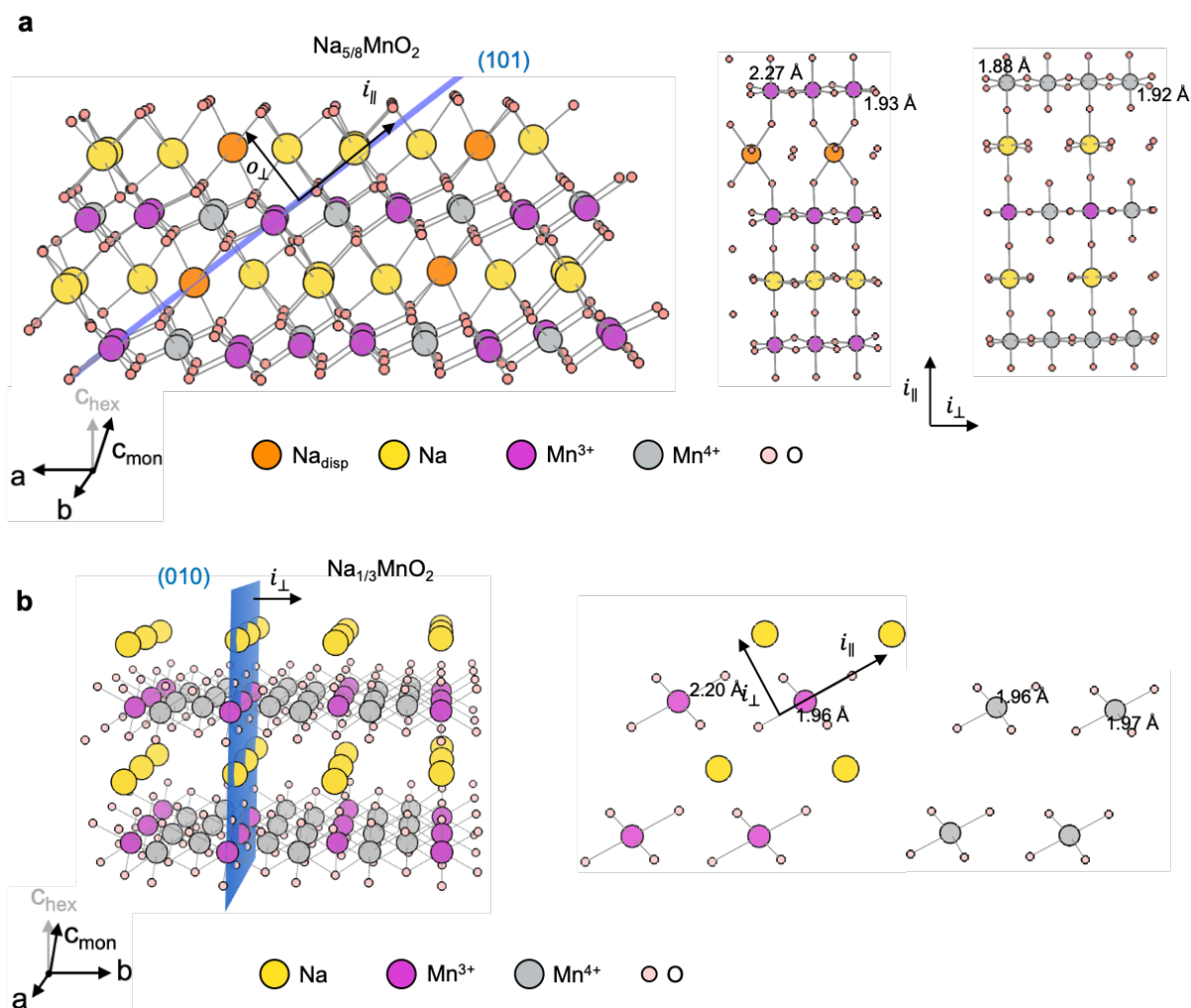**Figure S12. Structure models of Na$_{5/8}$MnO$_2$ (a) and Na$_{1/3}$MnO$_2$ (b).** Figures from left to right are 3D structure, pure Mn^{3+} plane and other alternating planes mixed with Mn^{3+}/Mn^{4+} for Na$_{5/8}$MnO$_2$ and pure Mn^{4+} for Na$_{1/3}$MnO$_2$, respectively. Blue plane in each 3D model marks the pure Mn^{3+} atomic plane. Note that in both *in-situ* SXRD refinements and DFT simulations, Na$_{5/8}$MnO$_2$ and Na$_{1/3}$MnO$_2$ show the strongly elongated JT distortion of Mn^{3+}O$_6$, same as δ^+-Na$_{1/2}$MnO$_2$ in DFT.
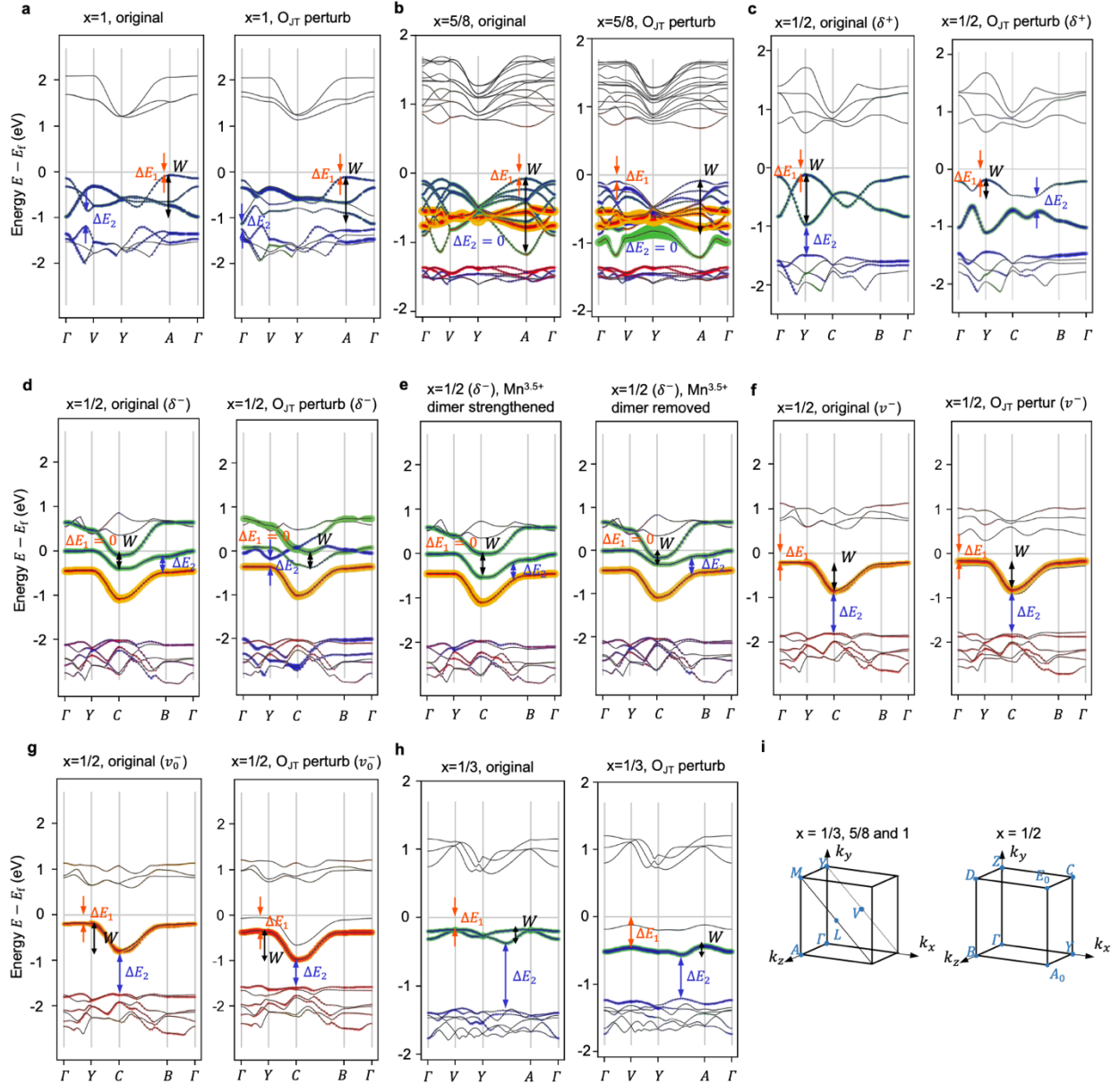
Figure S13. Original and perturbed band structures for Na$_x$MnO$_2$. (a) x = 1. (b) x = 5/8. (c-g) x = 1/2 (δ^+, δ^-, v^-, v_0^- states). (h) x = 1/3. The O$_{JT}$ perturbation is generated as the elongation of a pair of O$_{JT}$ ions by 0.1 Å along the JT long-axis directions of the elongation mode. The perturbations to the Mn$^{3.5+}$ dimer either shorten the dimer bond (strengthening dimerization) or elongate it (removing the dimer). Blue and green markers represent the band occupation of the Mn d and the O p orbitals in the JT active MnO$_6$ octahedron of the pure charge stripe, respectively. The color near E_f blends blue and green before perturbation, indicating a pd hybridization. At x = 1/2 (δ^+), 1/3 and 5/8, they are the d_{z^2} and the p_z orbitals of the two O$_{JT}$ oxygens that are hybridized to the Mn^{3+} ion, while at x = 1/2 (δ^-), they are the $d_{x^2-y^2}$ and p_x or p_y orbitals of the other four oxygens that hybridize to the Mn$^{3.5+}$ ion. At x=1/2, the orange and red markers represent the band occupation of the Mn^{3+} $d_{x^2-y^2}$ and the p_x or p_y orbitals of the four oxygens that hybridize with it, respectively, in the Mn^{3+}O$_6$ of Mn$^{3/4+}$ stripe; while at and x=5/8, they represent Mn^{3+} d_{z^2}

and the O_{JT} p_z orbitals, respectively, also in the mixed valence stripe. For v^- and v_0^- states at x = 1/2, we also use orange for Mn^{3+} ion and red for oxygen ion, indicating their negative JT distortion for $d_{x^2-y^2}$ and p_x / p_y orbitals. Note that for the δ^- state at x = 1/2 the JT distortion is different from the other three states at x = 1/2 and the two states at x = 1/3 and 5/8, due to its abnormal JT distortion with the weak compression on the unique $Mn^{3.5+}O_6$. However, for comparison, the perturbation in all three cases are generated on the same oxygen ions, i.e., the O_{JT} defined in x=1/3 and x=5/8, and along the JT long axes of the elongation mode. The O_{JT} perturbations are applied to one of the $Mn^{3+}O_6$ for x = 1, 1/2 (δ^+, v^-, v_0^-), 1/3; to one of the $Mn^{3+}O_6$ in the pure Mn^{3+} stripe at x = 5/8; to one of the $Mn^{3.5+}O_6$ at x = 1/2 (δ^-). The 3D diagrams show the corresponding Brillouin zone definition. $Na_{5/8}MnO_2$ shows the most obvious de-hybridization by perturbation, while $Na_{1/3}MnO_2$ shows an energy suppression to the perturbed d_{z^2} and p_z orbitals.
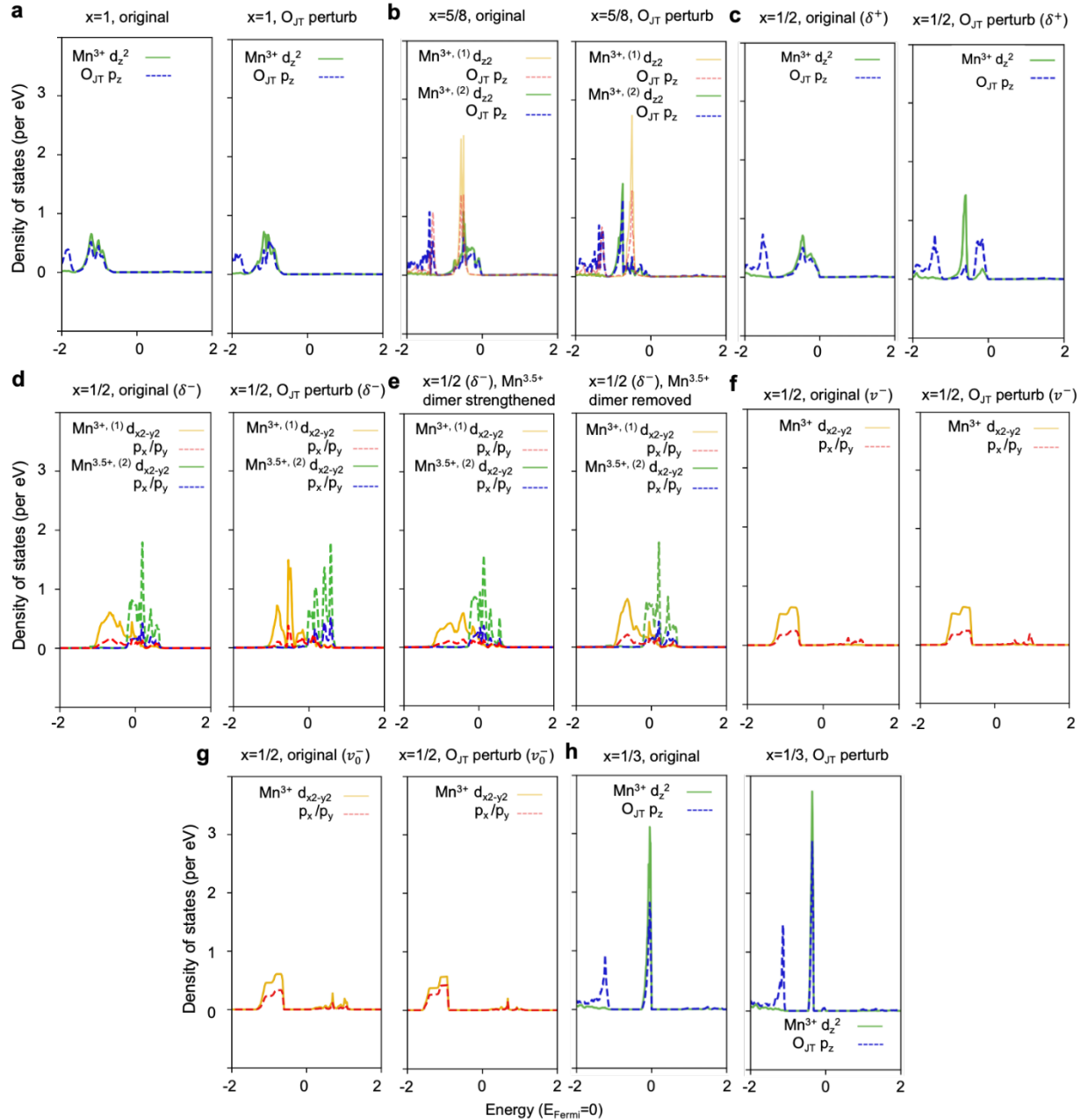
Figure S14. Original and perturbed DOS for Na$_x$MnO$_2$. (a) x = 1. (b) x = 5/8. (c-g) x = 1/2 (δ^+, δ^-, v^-, v_0^- states). (h) x = 1/3. The O$_{JT}$ perturbation is generated as the elongation of a pair of O$_{JT}$ ions by 0.1 Å along the JT long-axis directions of the elongation mode. The perturbations to the Mn$^{3.5+}$ dimer either shorten the dimer bond (strengthening dimerization) or elongate it (removing the dimer) in (e). The DOS of the p_z orbital of an elongated O$_{JT}$ and the d_{z^2} orbital of the Mn^{3+} in the octahedral center are plotted for x = 1/3. For x = 5/8, Mn$^{3+, (2)}$ is the Mn^{3+} in the pure Mn^{3+} stripe (Fig. S12) whose JT oxygens are elongated. Mn$^{3+, (1)}$ is the Mn^{3+} in the mixed Mn$^{3+/4+}$ plane/stripe. For the δ^- state at x = 1/2, the $d_{x^2-y^2}$ orbitals of the Mn$^{3.5+,(2)}$ in the Mn$^{3.5+}$ stripe, and Mn$^{3+, (1)}$ in Mn$^{3/4+}$ stripe, as well as p_x or p_y orbitals of the four non-O$_{JT}$ oxygens that hybridize with them are plotted. For the δ^+ state at x = 1/2, the d_{z^2} orbital for Mn^{3+} in the Mn^{3+} stripe, as well as

p_z orbitals of the two O_{JT} oxygens are plotted. For the v^- and v_0^- states at x = 1/2, we also use orange for Mn^{3+} ion and red for oxygen ion, indicating their negative JT distortions with $d_{x^2-y^2}$ and p_x / p_y orbitals. Note that for the δ^- state at x = 1/2 the JT distortion is different from the other three states at x = 1/2 and the two states at x = 1/3 and 5/8 due to its abnormal JT distortion with the weak compression on the unique $Mn^{3.5+}O_6$. However, for comparison, the perturbation in all three cases are generated on the same oxygen ions, i.e., the O_{JT} defined in x=1/3 and x=5/8, and along the elongated JT direction. The O_{JT} perturbations are applied to one of the $Mn^{3+}O_6$ for x = 1, 1/2 (δ^+, v^-, v_0^-), 1/3; to one of the $Mn^{3+}O_6$ in the pure Mn^{3+} stripe at x = 5/8; to one of the $Mn^{3.5+}O_6$ at x = 1/2 (δ^-).
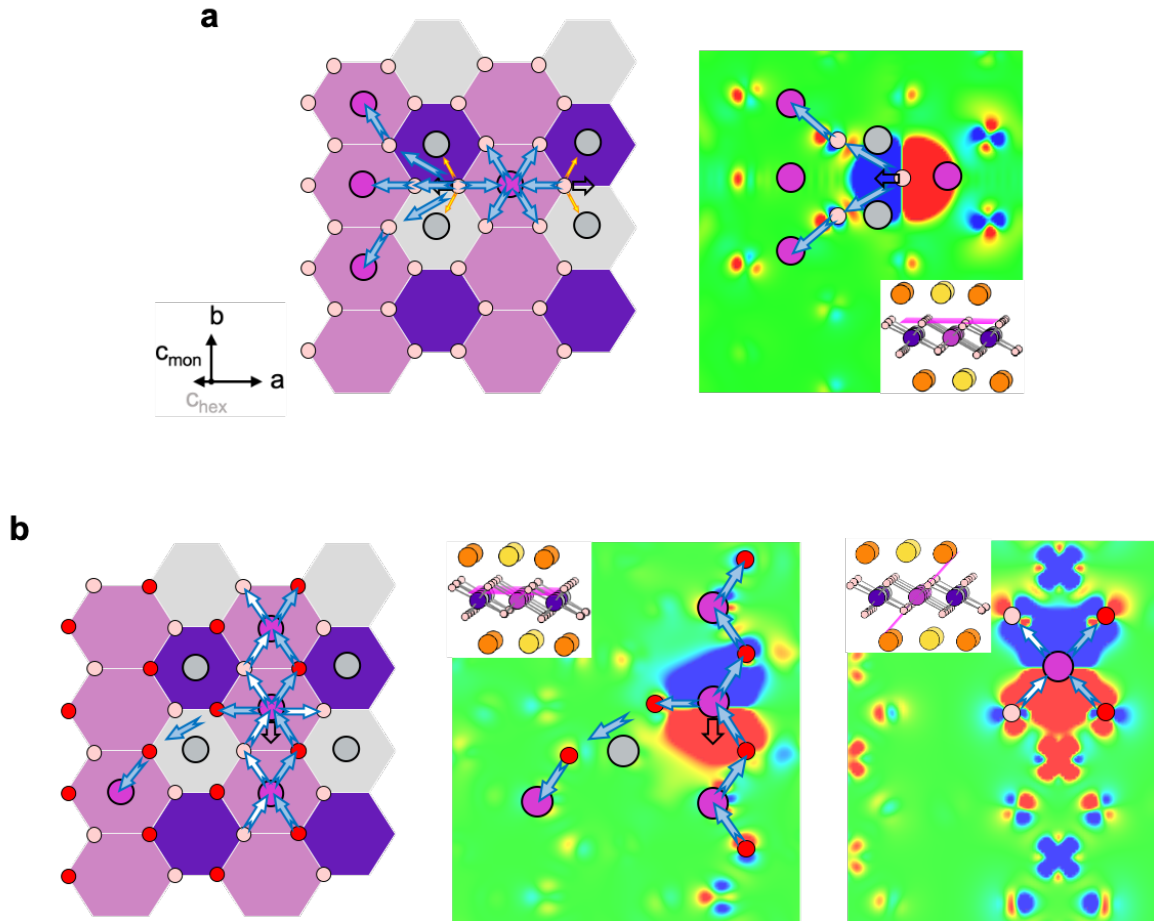
Figure S15. Charge density difference (CCD) resulted from the perturbation of ions for δ^--Na$_{1/2}$MnO$_2$. (a) Perturbation of a pair of O$_{JT}$ ions along the JT long-axis. (b) Perturbation of a Mn$^{3.5+}$ ion along the *b* direction. The result corresponds to Fig. 2(e) in the Main Text. More reddish and more blueish regions in CCD indicate larger amounts of electron increase and decrease, respectively. Blue arrows indicate charge flux flow directions, and black empty arrows indicate the ion perturbation direction. The section in (a) goes through the oxygen plane defined by the 3 oxygen ions in the CCD (inset), which clearly shows the charge fluxes from the perturbed O$_{JT}$ ions to the oxygens of the neighboring Mn$^{3.5+}$O$_6$ stripe. Multiple such CCD sections along different planes are needed in order to illustrate the entire flow pathways shown in (a, left). The section in (b) goes through the plane at the center between the Mn layer and O layer, and a plane including Mn and four oxygens as shown in the insets. It shows the zig-zag fluxes along the *b* direction, as well as across the Mn$^{3.5+}$ stipes. For clarity, only relevant ions are shown in the CCD plots. Note that here we illustrate some visual evidence of the charge fluxes. The actual charge flux direction and strength are determined by quantitative calculations using the entire 3D density.
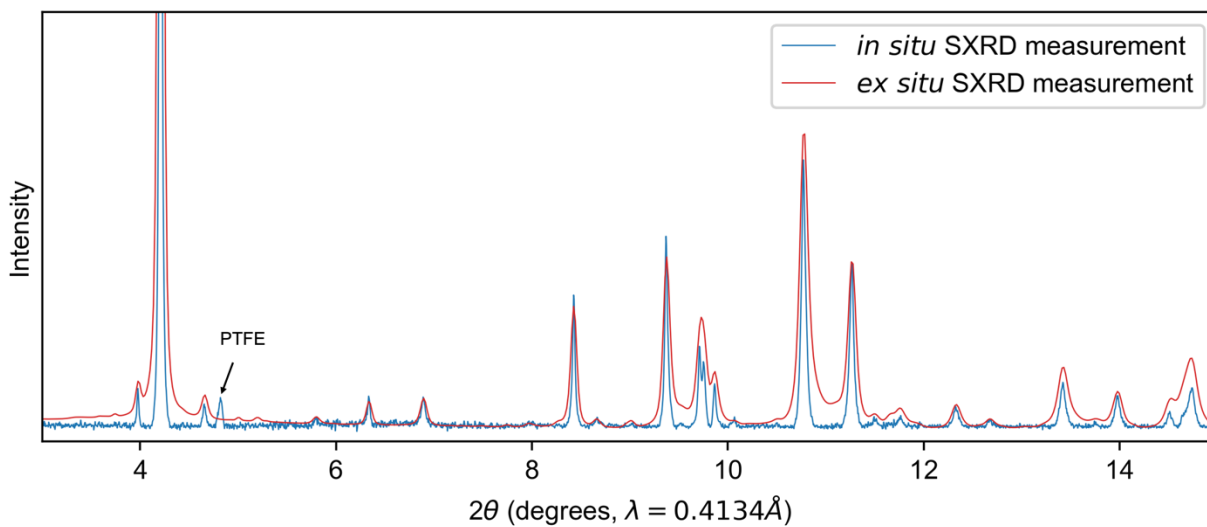
Figure S16. Comparison of *in-situ* SXRD (λ = 0.4134 Å) collected at 11-BM of APS at ANL and *ex-situ* SXRD (λ = 0.1844 Å) collected at 28-ID-2 of NSLS II at BNL for Na$_{1/2}$MnO$_2$. The plot for *ex-situ* SXRD is scaled to 0.4134 Å as well. Both SXRD patterns are after the background subtraction.
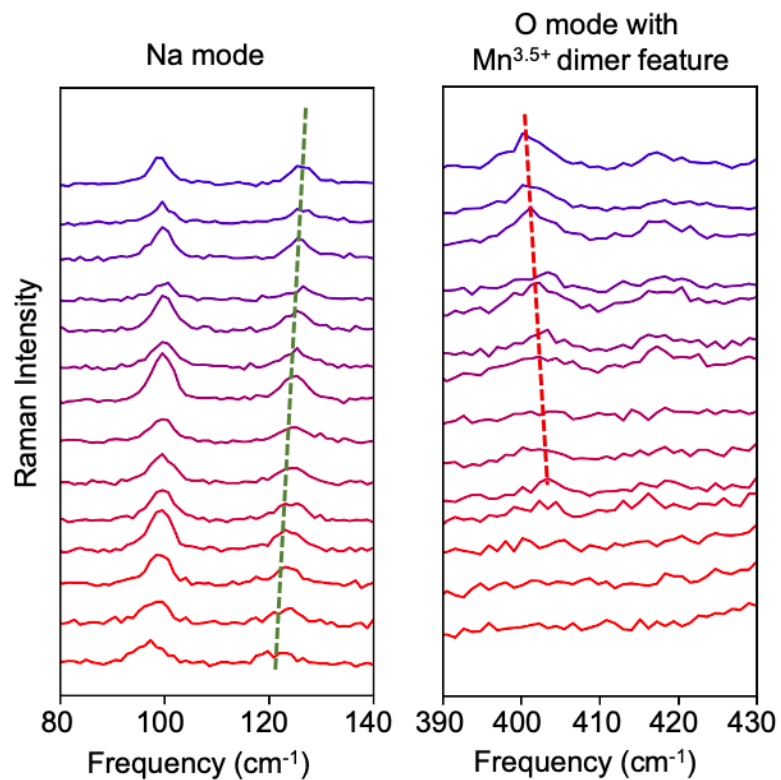
Figure S17. Zoom-in plots around the frequencies of the green and red arrows in Fig. 3(a). They represent for (left) the Na phonon modes, and (right) the oxygen phonon modes, from comparison with DFT simulations in Fig. S18 and S19.
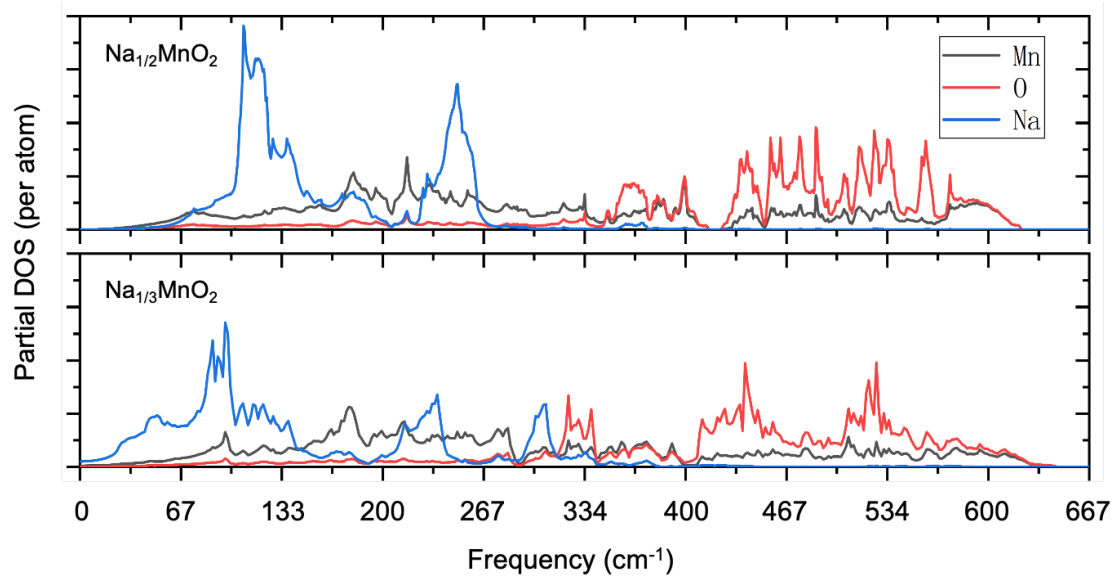
Figure S18. DFT calculated phonon spectra of Na$_{1/3}$MnO$_2$ and δ^--Na$_{1/2}$MnO$_2$.
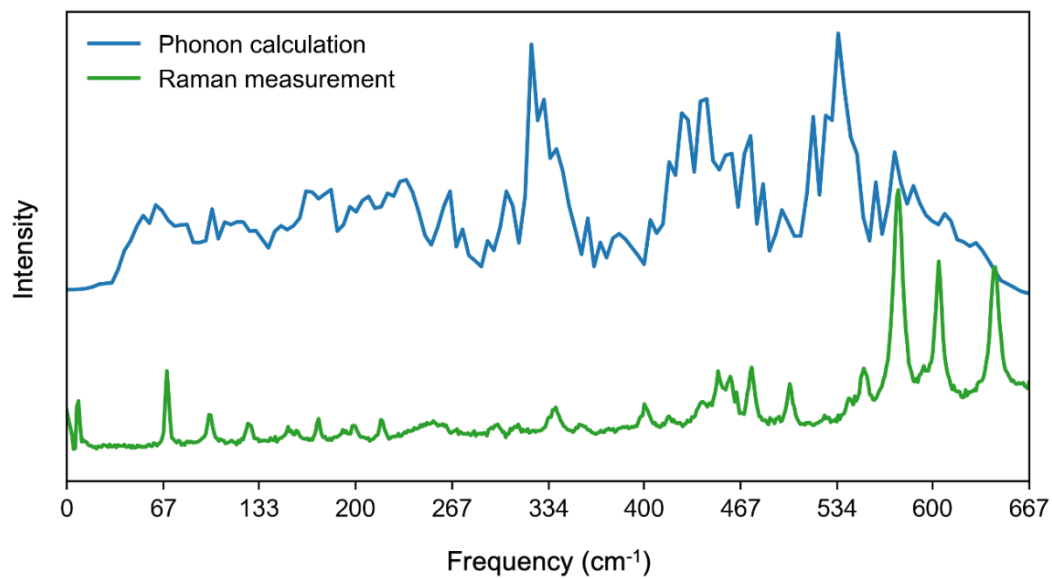
Figure S19. Comparison between the calculated phonon spectra of δ^--$Na_{1/2}MnO_2$ (blue) and the measured Raman spectra (green) for $Na_{1/2}MnO_2$.
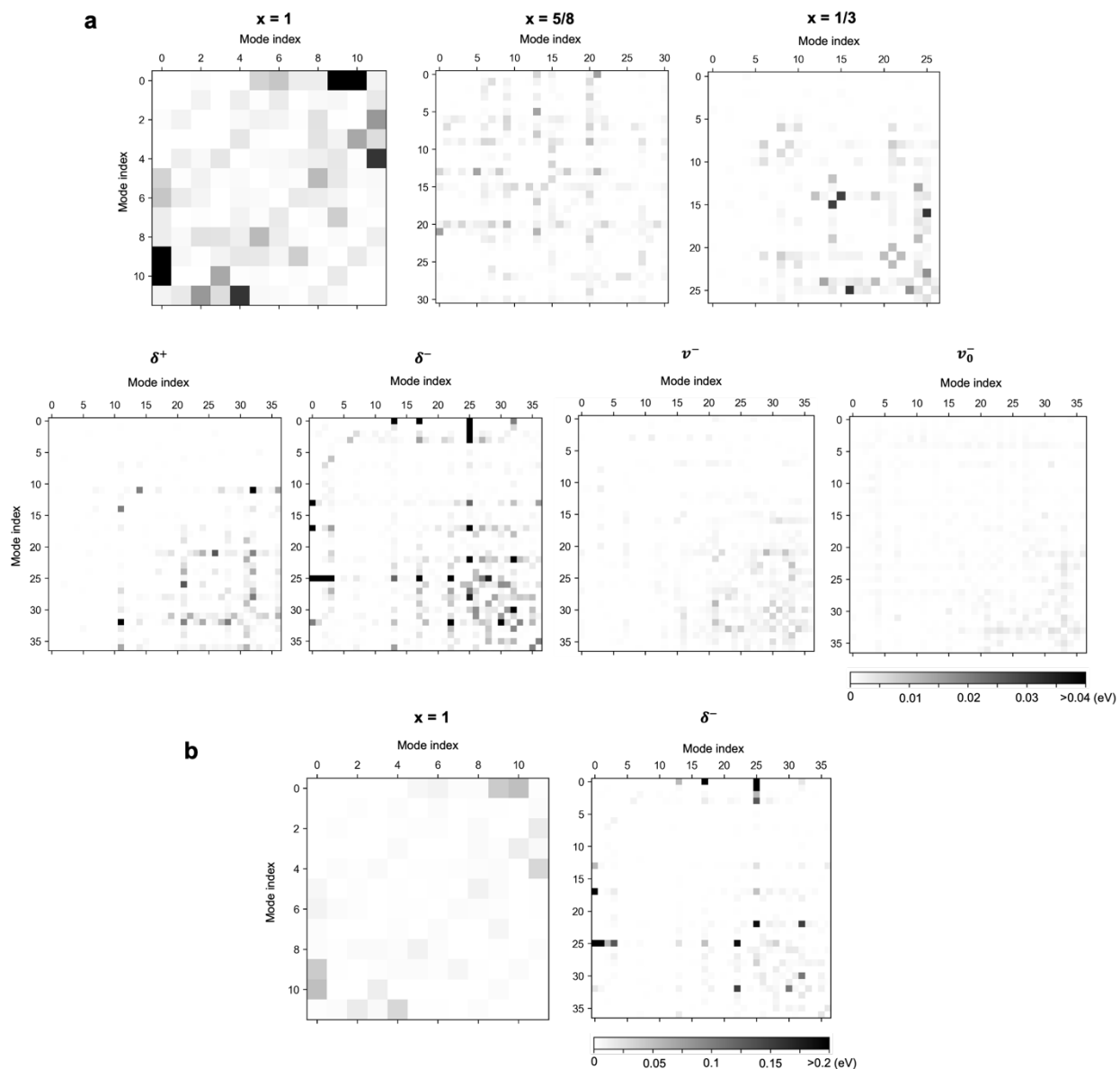
Figure S20. Phonon coupling map for Na$_x$MnO$_2$ states at x = 1, x = 5/8, x = 1/3 and δ^+, δ^-, ν^-, and ν_0^- states at x=1/2. Figure 3d of the Main Text is generated using these results. (a) comparison among all seven states with a high cutoff of 0.04 eV. (b) Comparison between x=1 and δ^- states with a high cutoff of 0.2 eV.
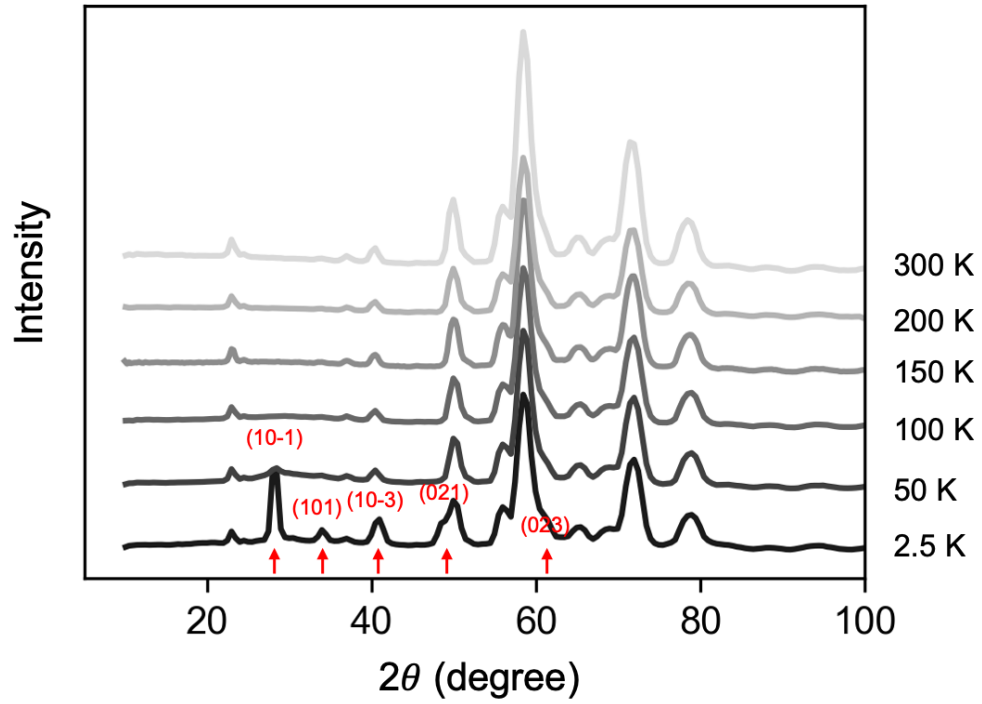
Figure S21. Neutron diffraction spectra measured at different temperatures from 2.5K to 300K for Na$_{1/2}$MnO$_2$. The red arrows indicate magnetic peaks marked with (hkl) labels.
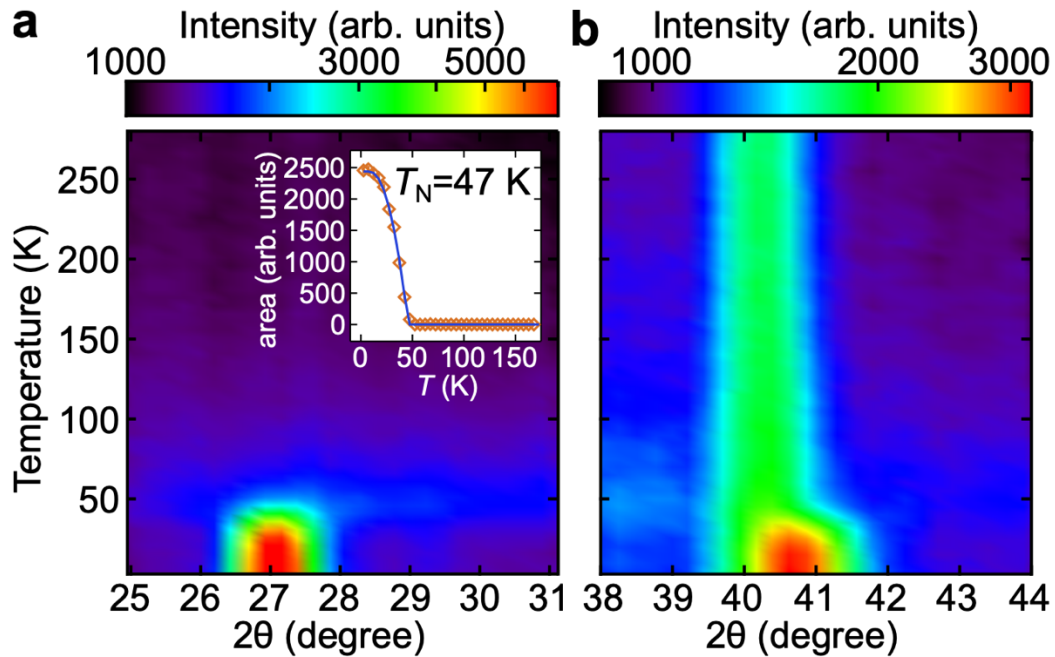
Figure S22. Heatmap of the evolution of neutron diffraction spectra with decreasing temperature in the 2θ angle ranges. (left) Measurement around the 10-1 Bragg magnetic peak. (right) Measurement around the 10-3 (right) Bragg magnetic peak. The plots correspond to Fig. 4b and 4c in the Main Text. The more reddish and blueish regions indicate stronger and weaker neutron signals, respectively. The inset shows the integrated intensity (square of the order parameter) versus temperature, with a mean field fit (solid curve) to estimate the Néel ordering temperature of 47(1) K.

a

b

	$|J|$ (K)	J (meV)
$J_{33}^{(1)}$	174	15.0
$J_{34}^{(1)}$	106	9.1
$J_{33}^{(2)}$	163	-14.1
$J_{34}^{(2)}$	119	-10.3
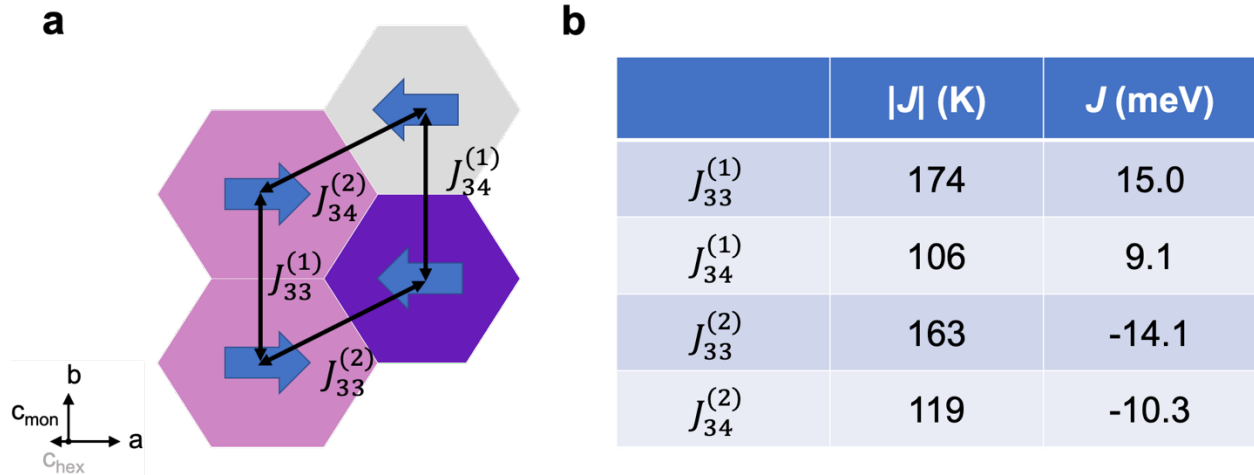
Figure S23. DFT prediction of ground state magnetic ordering and calculated magnetic coupling constants $J_{ij}^{(n)}$ in δ^{-}-Na$_{1/2}$MnO$_2$. (a) ground state magnetic ordering. (b) calculated magnetic coupling constants. The subscript 3 indicates it is Mn^{3+} or Mn$^{3.5+}$ that participates in the coupling, and 4 indicates it is Mn^{4+}, while the superscript indicates the inequivalent interactions. Positive J means ferromagnetic coupling and negative means antiferromagnetic coupling. The ground state magnetic ordering in (a) from DFT prediction is consistent with neutron refinement.
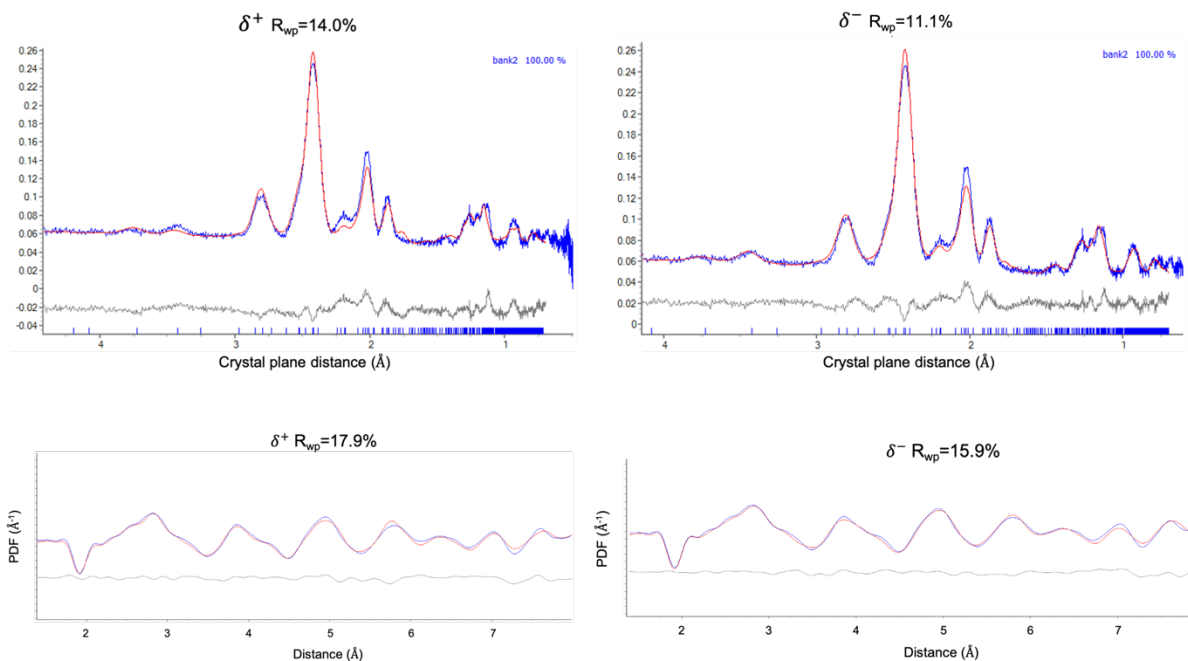
Figure S24. Neutron diffraction and neutron PDF refinements of δ^+ and δ^- states at x = 1/2 for Na$_x$MnO$_2$. (top) Neutron diffraction refinements. (bottom) Neutron PDF refinements.

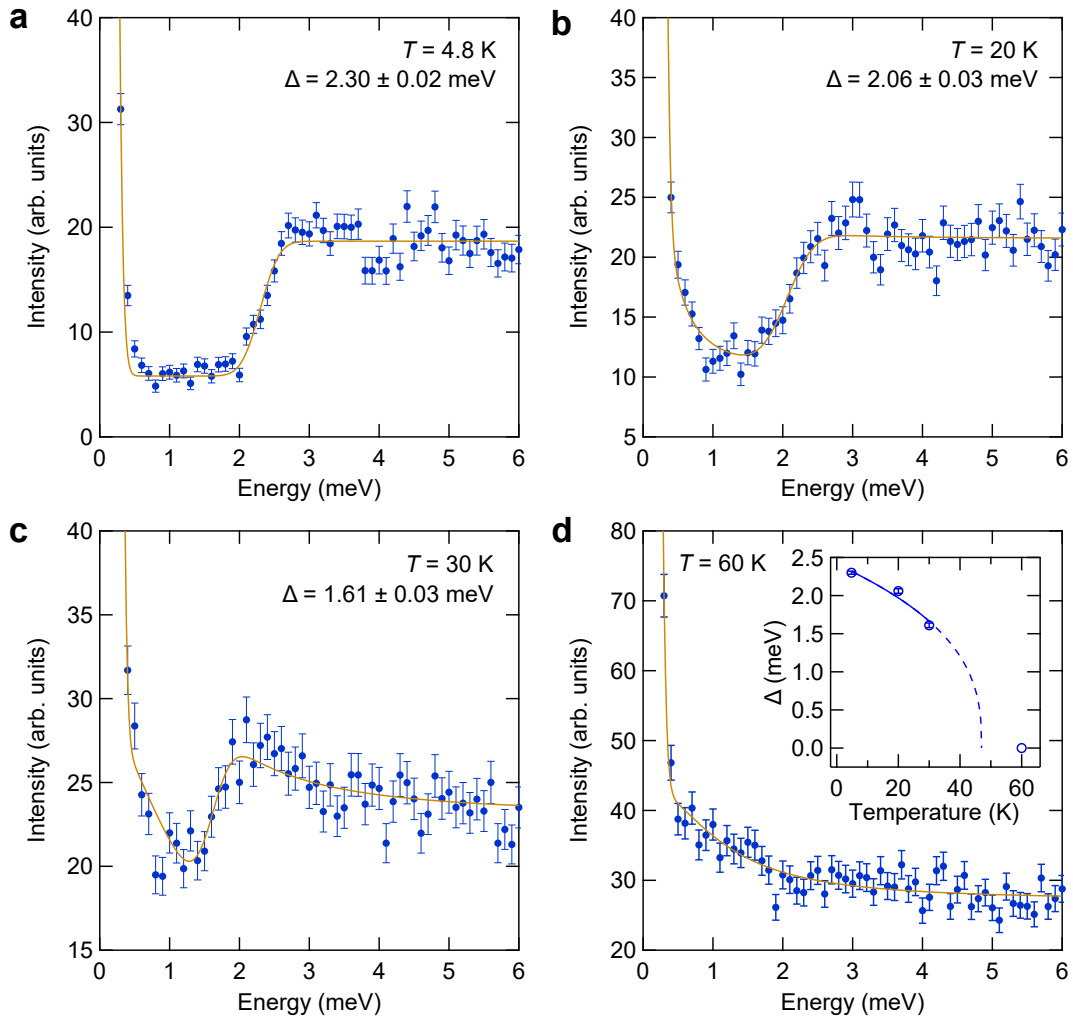**Figure S25**. **Inelastic neutron scattering of the magnon spectra at the magnetic zone center of Na$_{1/2}$MnO$_2$**. (a)T = 4.8 K. (b) T = 20 K. (c) T = 30 K. (d) T = 60 K. Δ denotes the gap value. The solid curves are the fits to a step function at the gap energy plus intrinsic lifetime broadening and a delta function at zero energy for the elastic scattering, convoluted with the instrumental resolution. At base temperature a sharp gap of 2.30 meV is observed. With increasing temperature, the gap softens, the magnetic scattering broadens, and by 60 K the gap has closed, and only quasi-elastic scattering is found. The inset in (d) shows the temperature dependence of the gap and the solid-dashed blue curve is fitted using $(T_N - T)^{1/3}$ power law assuming the gap is zero at T$_N$.
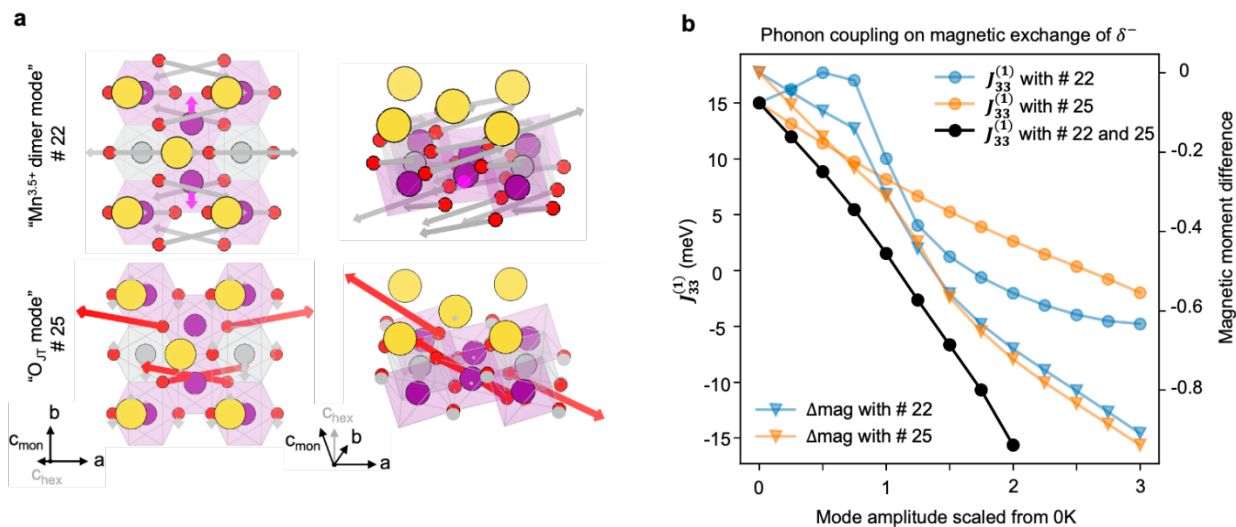
Figure S26. Typical phonon modes and their effect on magnetic coupling strength $J_{33}^{(1)}$. (a) Illustration of phonon modes # 22 and 25 in Fig. 3c. Vectors are scaled movements of atoms. Purple and red vectors highlight the special $Mn^{3.5+}$ dimer component and the elongation O_{JT} component. Note: 1 meV = 8.065 cm^{-1}. (b) Magnetic coupling strength $J_{33}^{(1)}$ of the δ^- state between nearest $Mn^{3.5+}$ ions along *b* vs. applying phonon mode amplitudes of $Mn^{3.5+}$ dimer mode (# 22, blue dots), O_{JT} mode (# 25, orange dots) and both modes together (black dots) to the δ^- structure, respectively. The two modes are applied together based on the calculated anharmonic coupling phase. The blue and orange triangles are the phonon induced transient magnetic moment difference between the two dimer $Mn^{3.5+}$ ions in the $Mn^{3.5+}$ *b* stripe.
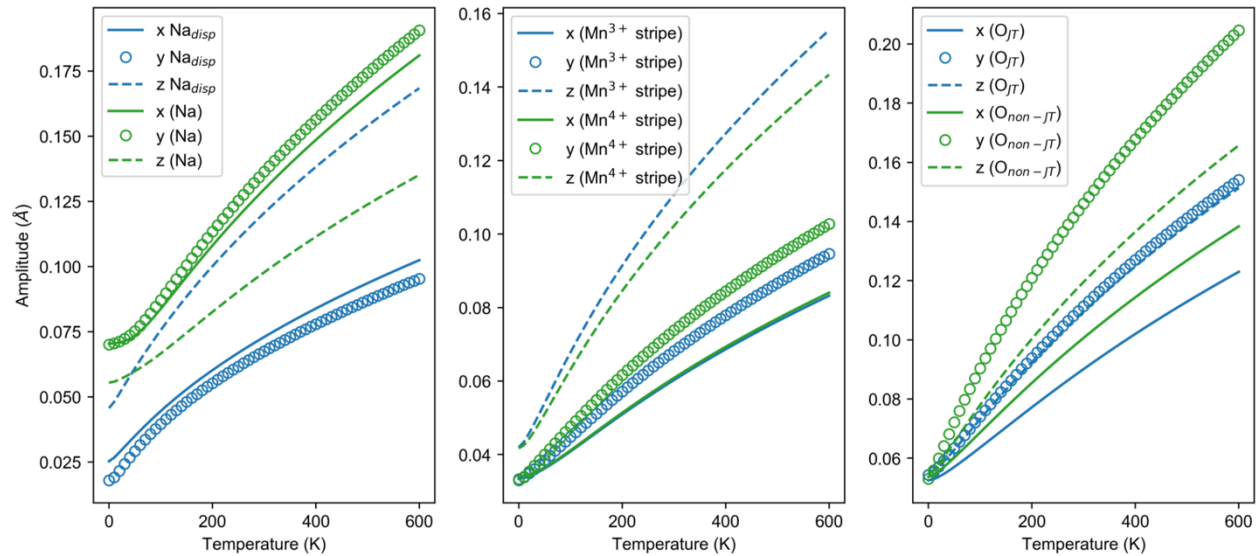
Figure S27. The average oscillation amplitude of each ion in δ^--Na$_{1/2}$MnO$_2$ along x, y, and z directions versus temperature based on the DFT calculated phonon spectra.
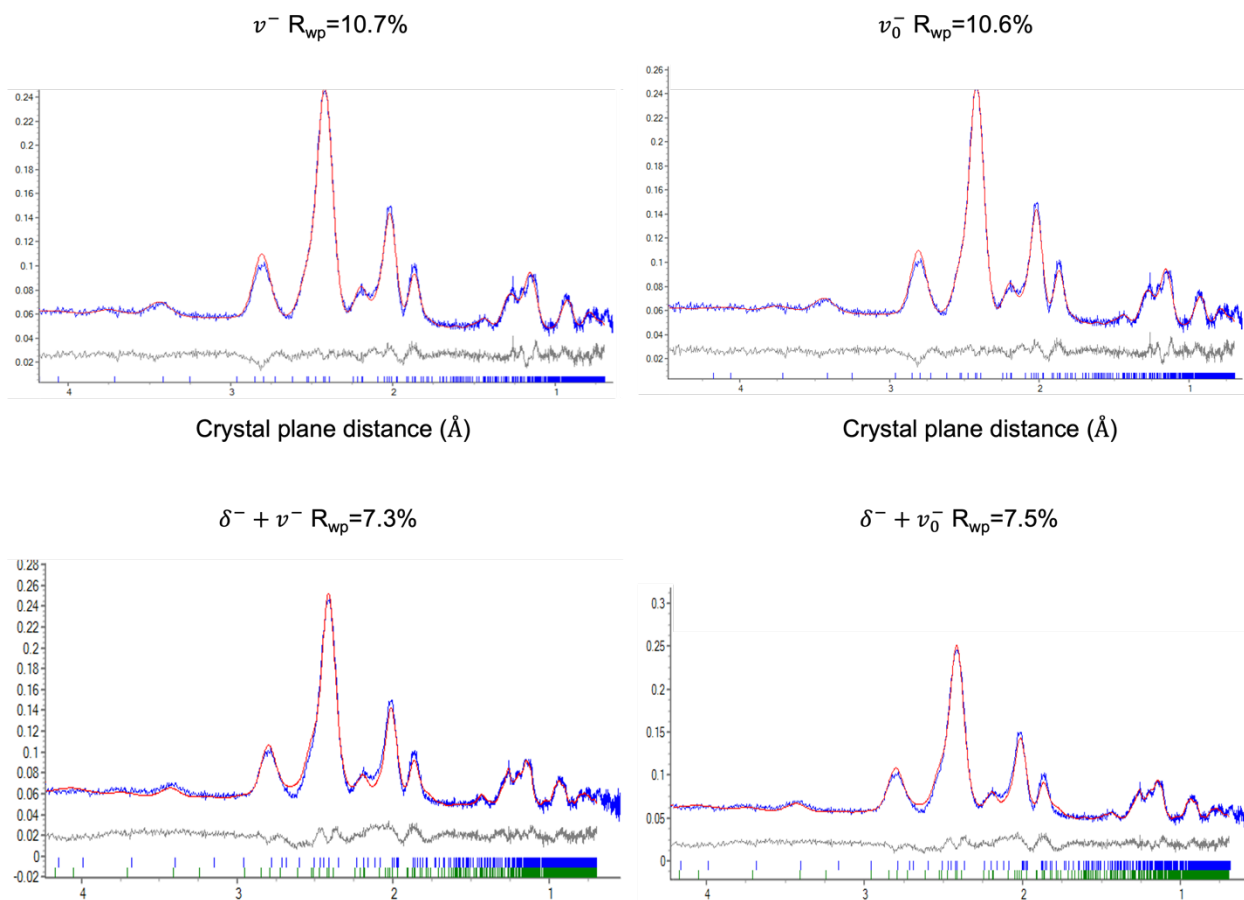
Figure S28. Neutron diffraction refinements. (top) v^- and v_0^- states at x = 1/2 Na_xMnO_2. (bottom) two-phase diffraction refinements of $\delta^- + v^-$ and $\delta^- + v_0^-$.
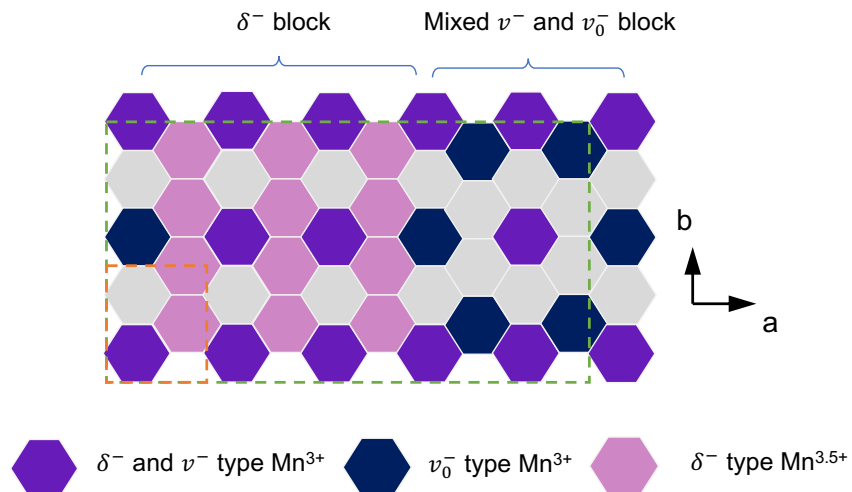
δ^- block ⟶ | ⟵ Mixed v^- and v_0^- block

b ↑
a →

δ^- and v^- type Mn^{3+} v_0^- type Mn^{3+} δ^- type $Mn^{3.5+}$

Figure S29. One possible Na$_{1/2}$MnO$_2$ large supercell that combines blocks of δ^- and mixed v^-/v_0^- regions to better refine SXRD. Mn valence ordering pattern in a larger supercell (green rectangle) with δ^- type and mixed v^-/v_0^- type Na ordering regions alternating along *a* direction and with the cell size doubled along *b* direction. The orange rectangle shows the primitive cell size corresponding to the four DFT low-energy states in Na$_{1/2}$MnO$_2$ (Fig. 1b).
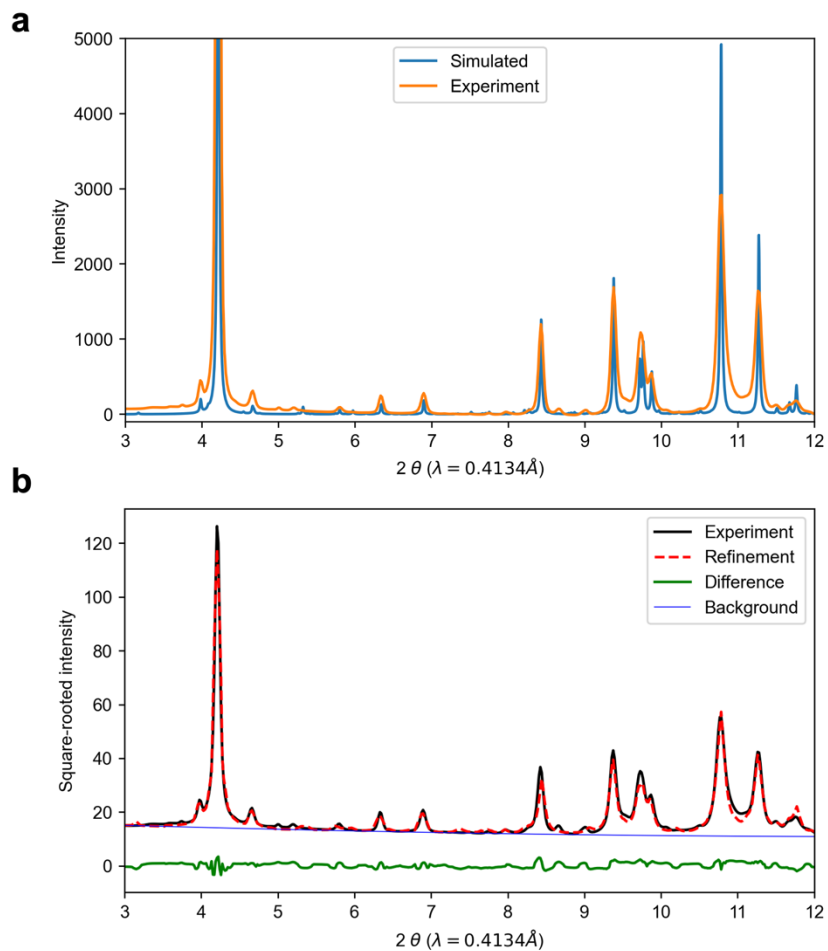
Figure 30. XRD simulation and refinement based on an enlarged supercell with blocks of δ^- type and ν^-/ν_0^- type Na orderings alternating along *a* direction and with the cell size doubled along *b* direction. (a) Simulated XRD vs experiment. (b) Rietveld refinement. The thermal displacement parameter B_{eq} in the refinement is fitted within the [-0.5, 0.5] range.